Supplementary Information

Plasma radicals control platinum supported nitrogen doped graphitic carbon formation for ambient pressure ammonia synthesis

Jiangqi Niu, Shan Ding, Xu Ma, Zheng Lian, Chayanaphat Chokradjaroen, Shijie Xian, Sana Ullah, Xiaohan Chen, Yunxia Yang, Rusen Zhou, Renwu Zhou, Anthony B. Murphy, Xiaolei Fan, Yiguang Ju, Bruce C. Gates, Sibudjing Kawi

*Corresponding authors' e-mail: xiaolei.fan@manchester.ac.uk (X.F.); yju@princeton.edu (Y.J.); bcgates@ucdavis.edu (B.C.G.); chekawis@nus.edu.sg (S.K.)

The PDF file includes:

Other Supplementary Materials for this manuscript include the following:

Supplementary Note 1.

Time-resolved microsecond imaging was used to capture the discharge evolution in the biphasic liquid–liquid plasma reactor. The discharge proceeded through a repeated bubble-confined ignition process at the liquid–liquid interface. At approximately 10–20 μs after pulse initiation, transient gas microbubbles appeared near the interface beneath the high-voltage electrode. These bubbles likely originated from localized heating, vaporization, and electron-impact dissociation and ionization processes occurring near the electrode–liquid and plasma–liquid interfaces.

Between approximately 20 and 40 μs, plasma breakdown occurred within the transient bubble swarm, as indicated by the sudden appearance of a bright luminous region. The emission region then expanded rapidly, filling the bubble-occupied volume and extending toward the surrounding liquid interface. This observation indicates that the transient bubbles served as low-density discharge channels, facilitating electrical breakdown at the liquid-liquid interface.

At approximately 40–60 μs, the emission intensity decreased as the transient plasma channel collapsed. The system then returned to the initial state before the next voltage pulse initiated another equivalent discharge event. Because the discharge was driven at 30 kHz, this sequence was repeated periodically during plasma operation.

These observations indicate that the discharge was governed by the coupled effects of interfacial confinement and bubble-assisted breakdown. The liquid–liquid interface restricted the discharge to a narrow region and stabilized the plasma spatially, while the transient bubbles provided low-density regions that lowered the breakdown threshold and guided discharge-channel formation. As a result, the reactor sustained stable, repeatable, bubble-confined microdischarges at sub-ampere currents, avoiding the formation of continuous arcs or bulk liquid plasma channels. This discharge mode provides a controlled, low-current, nonthermal plasma environment at the liquid–liquid interface, which is favorable for rapid precursor activation, carbonization, and nitrogen retention.

Supplementary Note 2

Determination of DBD discharge power and calculation of ammonia energy yield.

The discharge power in the dielectric barrier discharge (DBD) reactor was determined using the standard Q–V Lissajous-figure method. In a DBD, the electrical energy delivered to the discharge per excitation period equals the closed-loop area of the charge–voltage (Q–V) trajectory. The average discharge power is then obtained by multiplying this energy per cycle by the excitation frequency. Direct measurement of the charge transferred in a DBD is not straightforward, because the current contains both displacement (capacitive) components and short microdischarge pulses. To quantify $Q(t)$ robustly, a known capacitor C_m was inserted in series with the DBD reactor as a charge monitor. In a series circuit, the same current flows through the monitor capacitor and the DBD at any instant. The charge passing through the circuit is therefore equal to the charge accumulated on the monitor capacitor:

$$Q(t) = C_m V_m(t) \quad \text{S1}$$

where $V_m(t)$ is the measured voltage across the monitor capacitor. Consequently, the current can be expressed as

$$I(t) = \frac{dQ(t)}{dt} = C_m \frac{dV_m(t)}{dt} \quad \text{S2}$$

In practice, $V(t)$ (the applied voltage across the DBD reactor) and $V_m(t)$ were recorded simultaneously. The Q–V plot was then constructed by using $Q(t)=C_m V_m(t)$ as the vertical axis and $V(t)$ as the horizontal axis, with the loop area giving E_{cycle}. This approach inherently includes both displacement and microdischarge contributions to charge transfer and is therefore well suited for power determination in filamentary DBD operation.

For any electrical system, the instantaneous power is $p(t)=V(t)I(t)$. The energy deposited over one excitation period T is

$$E_{cycle} = \int_0^T V(t)I(t)dt \quad \text{S3}$$

Because $I(t)=dQ(t)/dt$, this can be rewritten as

$$E_{cycle} = \int_0^T V(t)\frac{dQ(t)}{dt}dt = \oint V dQ \quad \text{S4}$$

which is exactly the enclosed area of the Q–V Lissajous loop. Therefore, the time-averaged discharge power is

$$P_{discharge} = fE_{cycle} = f\oint V dQ \quad \text{S5}$$

where $f = 1/T$ is the excitation frequency.

Ammonia energy yields (E) were calculated

$$E_{NH3} = \frac{\dot{n}_{NH3} M_{NH3}}{P_{discharge}} \quad \text{S6}$$

Supplementary Note 3

DFT calculation details.

Density functional theory calculations were performed with the Vienna Ab initio Simulation Package (VASP). The projector-augmented wave method was used to describe ion–electron interactions[1,2], and the Perdew–Burke–Ernzerhof functional within the generalized gradient approximation was used for exchange–correlation energies[3]. Spin polarization was included in all calculations. The N-doped graphene surface was modeled with a 7 × 7 × 1 periodic slab. A 20 Å vacuum layer was introduced along the z direction to minimize interactions between periodic images. The plane-wave cutoff energy was 500 eV. Structures were relaxed until the total-energy change was below 10^{-5} eV atom^{-1} and the residual force[4] was below 0.02 eV Å^{-1}.

The adsorption energy was calculated as:

$$E_{ads} = E_{total} - E_{slab} - E_{adsorbate} \quad \text{S7}$$

where E_{total} is the total energy of the optimized adsorbate–slab system, E_{slab} is the energy of the optimized slab, and $E_{adsorbate}$ is the energy of the isolated adsorbate. The Gibbs free-energy change was calculated following the Nørskov approach:

$$\Delta G = \Delta E + \Delta E_{ZPE} - T\Delta S \quad \text{S8}$$

where ΔE is the DFT energy difference, ΔE_{ZPE} is the zero-point energy correction, T is the temperature, and ΔS is the entropy change. The temperature was set to 298.15 K.

The binding energy of Pt single atoms or Pt clusters on N-doped graphene was calculated as:

$$E_{bind} = E_{Pt-slab} - E_{slab} - E_{Pt} \quad \text{S9}$$

where $E_{Pt-slab}$ is the total energy of the Pt-bound slab, E_{slab} is the energy of the corresponding slab, and E_{Pt} is the energy of the isolated Pt atom or Pt cluster.

The formation energy of Pt atoms or clusters anchored at N or C sites was calculated as:

$$E_f = E_{Pt-slab} - E_{slab} - E_{Pt,bulk} \quad \text{S10}$$

where $E_{Pt-slab}$ is the total energy of the Pt-containing slab, E_{slab} is the energy of the corresponding slab, and E_{Pt}, bulk is the reference energy of Pt in bulk Pt. A negative formation energy indicates that the corresponding configuration is thermodynamically favored.

The calculations included H_2 and N_2 dissociation on isolated Pt atoms and Pt clusters, nitrogen-reduction energy profiles on N-doped graphene, Pt single atom/N-doped graphene, Pt cluster/N-doped graphene, and coupled Pt single atom–Pt cluster/N-doped graphene models. The thermodynamic feasibility of N-vacancy refilling in Pt–N_x–C motifs was also examined. Crystal orbital Hamilton population analysis was used to evaluate Pt–N and Pt–C bonding for Pt single atoms and Pt clusters.

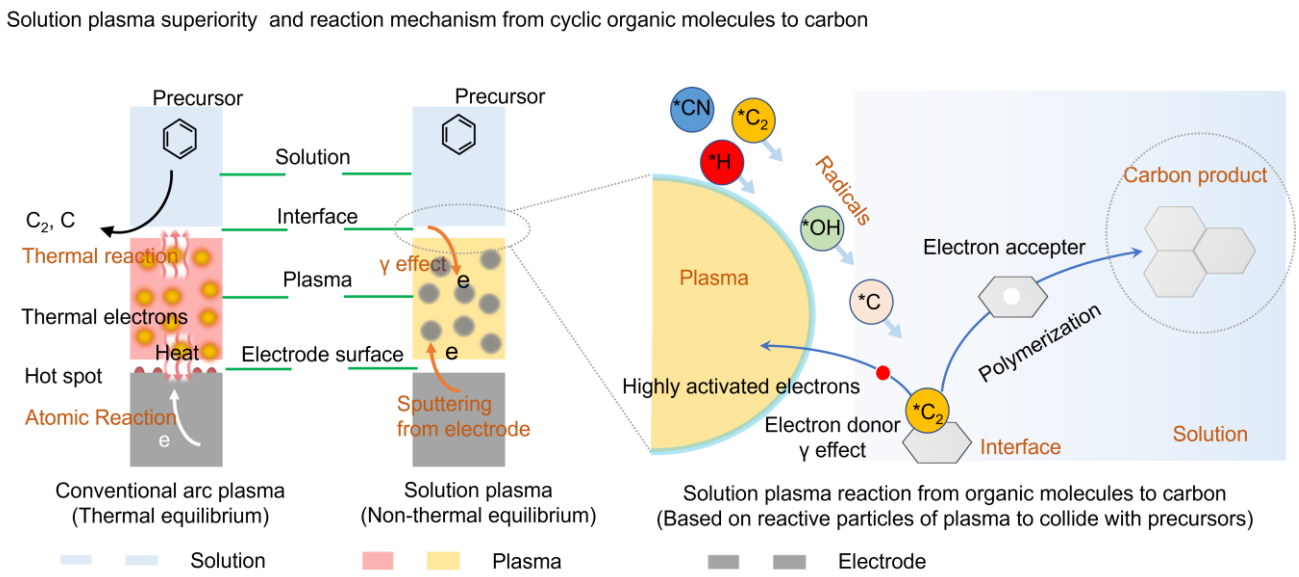

Figure S1. Comparison of carbon formation mechanisms in thermal arc plasma and solution plasma. In conventional arc plasma, carbon formation is mainly driven by thermal and atomic reactions associated with hot spots and thermal electrons. In solution plasma, non-thermal electron-induced processes, including the γ effect and electrode sputtering, promote the generation of highly activated electrons and reactive species at the plasma–solution interface. These species interact with cyclic organic precursors through electron-transfer and radical-mediated reactions, followed by polymerization toward carbon formation.

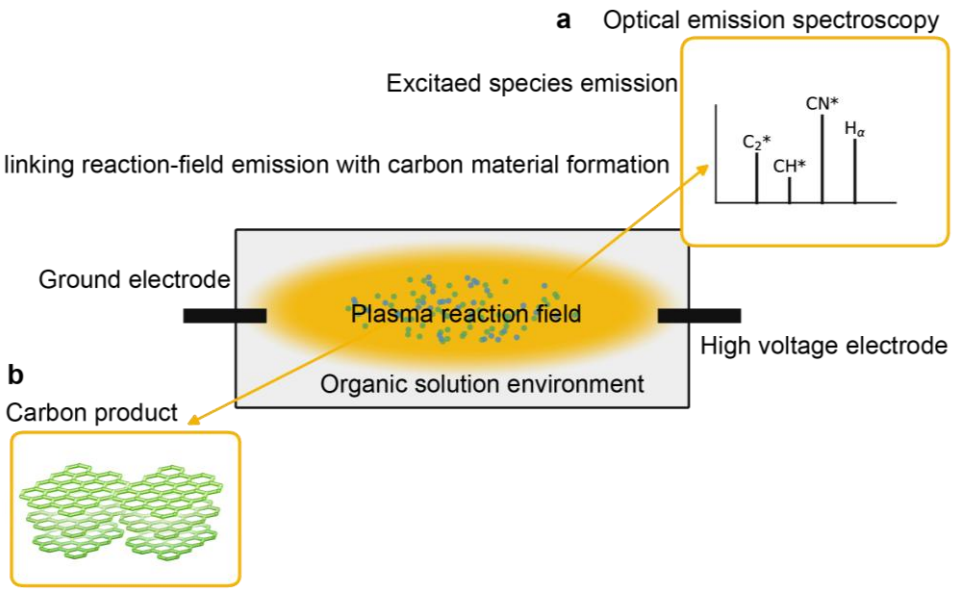

Figure S2. Schematic illustration of the solution plasma environment and emission–reaction correlation. (a) Discharge environment and location of plasma emission within the liquid phase. (b) Spatial relationship between the plasma reaction field and carbon formation zone.

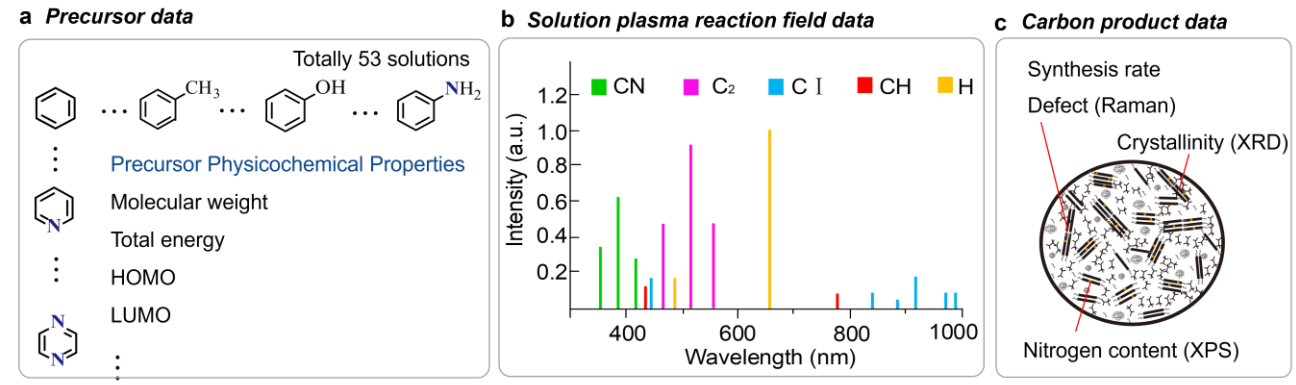

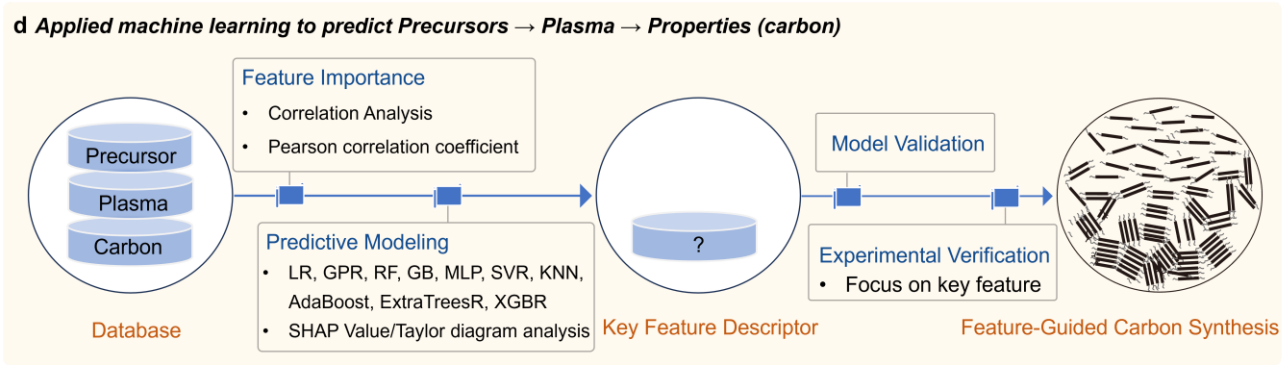

Figure S3. Integrated framework linking precursor chemistry, plasma emission, and carbon properties. (a) Dataset of 53 molecular precursors and their physicochemical parameters. (b) Representative optical emission spectra of reactive species in the solution plasma. (c) Characterization parameters of resulting carbon products, including synthesis rate, crystallinity (determined by XRD), defect density (determined by Raman spectroscopy), and nitrogen content (determined by XPS). (d) Machine-learning workflow connecting precursor–plasma–carbon data through correlation analysis and predictive modeling, enabling feature identification and model validation.

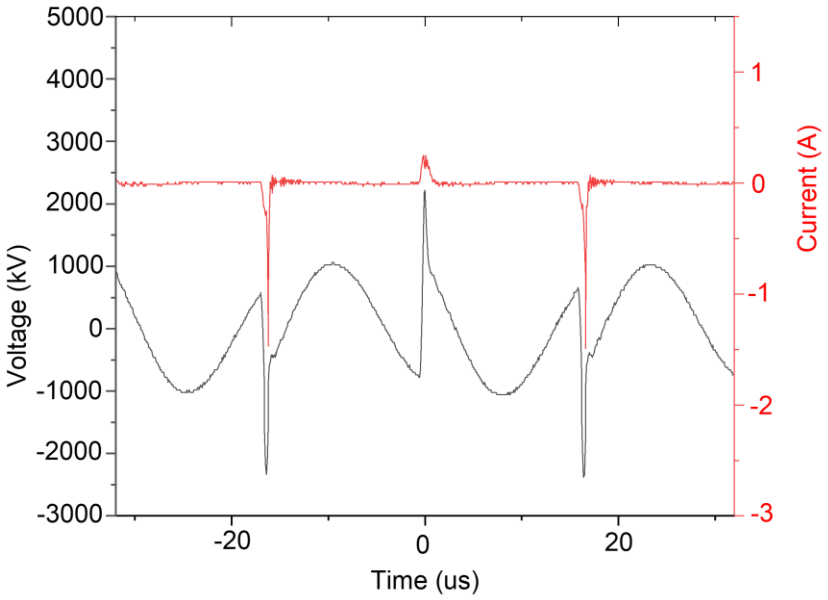

Figure S4. Voltage–current waveforms of the double-layer solution plasma. Representative voltage and current waveforms recorded during double-layer solution plasma discharge under the following conditions: applied voltage of 2 kV, pulse frequency of 30 kHz, pulse width of 1 μs, Cu electrodes with a 5 mm gap, and 200 mL of precursor solution. The plasma treatment duration was 45 min.

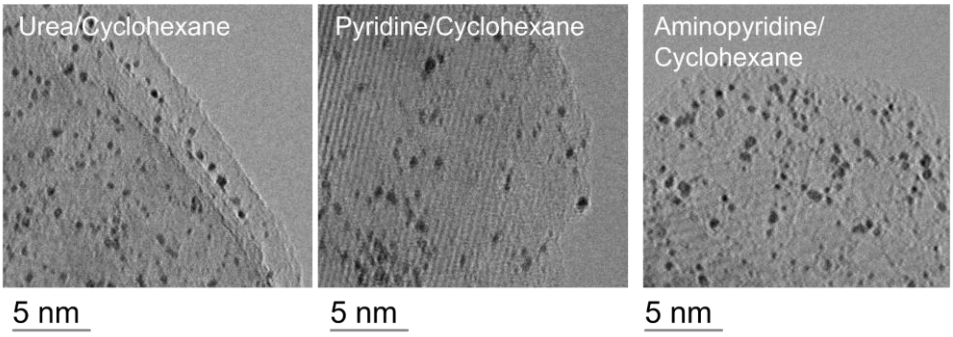

Figure S5. HRTEM images of carbon samples synthesized from different precursor systems. Representative HRTEM images of carbon samples obtained from urea/cyclohexane, pyridine/cyclohexane, and aminopyridine/cyclohexane precursor systems.

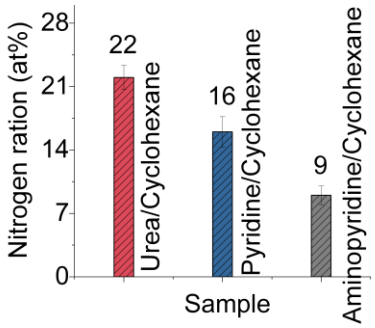

Figure S6. Nitrogen content of precursor-derived carbons. Elemental-analysis results for carbons synthesized from urea/cyclohexane, pyridine/cyclohexane, and aminopyridine/cyclohexane.

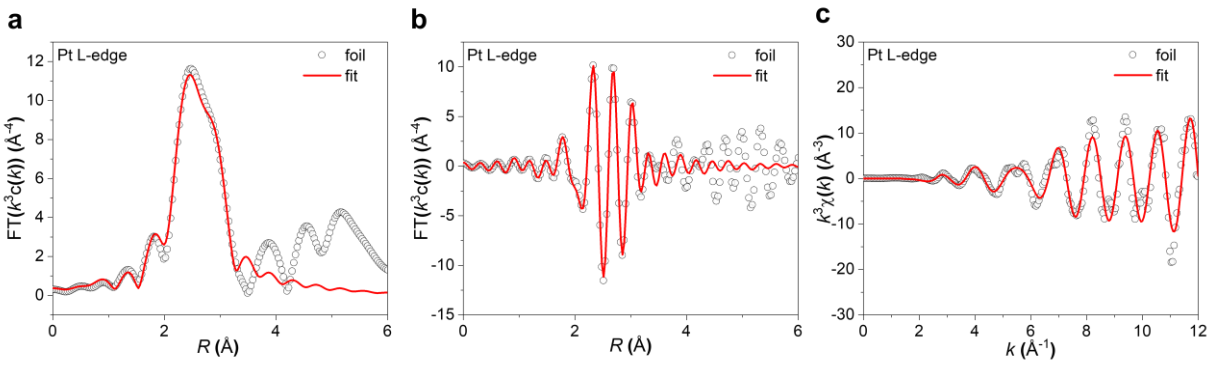

Figure S7. EXAFS fitting results characterizing Pt foil at the Pt L_3-edge. (a) R (distance)-space magnitude of the Fourier-transformed EXAFS spectra; (b) imaginary part of the R-space EXAFS fitting; (c) k^3-weighted $\chi(k)$ fitting in k-space (k is the wavenumber; $\chi(k)$ is the EXAFS function). Open symbols represent experimental results, and red lines correspond to the best fits.

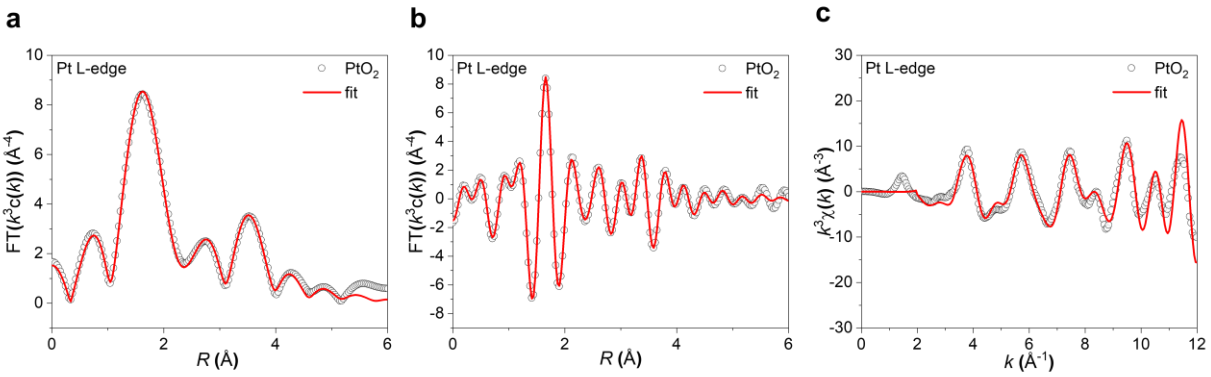

Figure S8. EXAFS fitting results of PtO_2 at the Pt L_3-edge. (a) *R*-space magnitude of the Fourier-transformed EXAFS spectra; (b) imaginary part of the *R*-space EXAFS fitting; (c) k^3-weighted $\chi(k)$ fitting in k-space. Open symbols represent experimental results, and red lines correspond to the best fits.

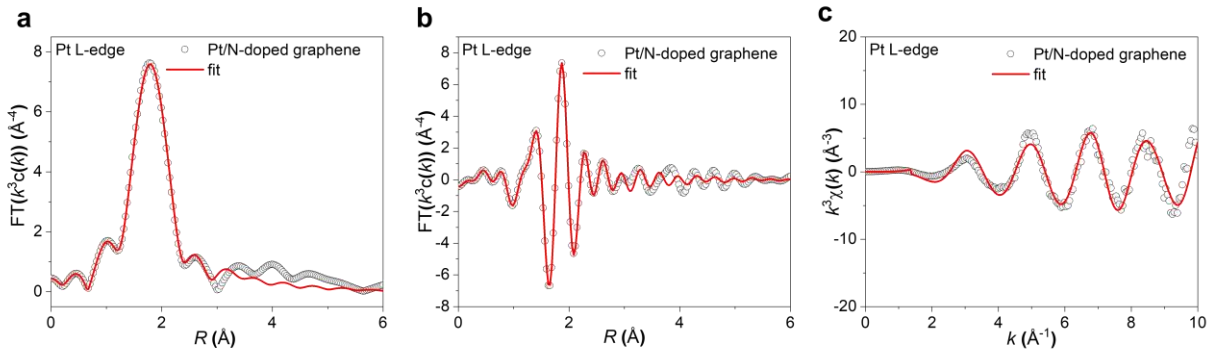

Figure S9. EXAFS fitting results of Pt@N-doped graphene at the Pt L_3-edge. (a) *R*-space magnitude of the Fourier-transformed EXAFS spectra; (b) imaginary part of the *R*-space EXAFS fitting; (c) k^3-weighted $\chi(k)$ fitting in *k*-space. Open symbols represent experimental results, and red lines correspond to the best fits.

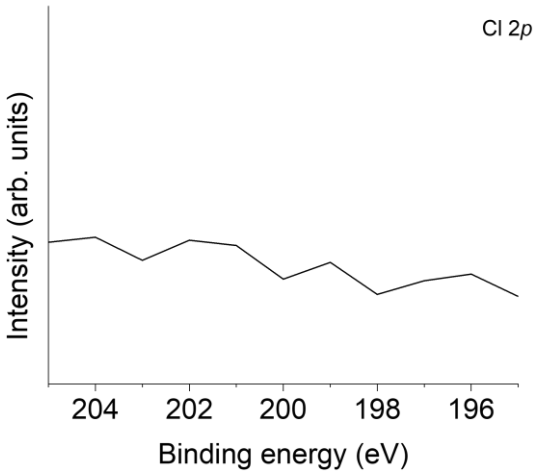

Figure S10. Cl 2*p* XPS spectrum. No distinct Cl 2*p* signal is observed in the analyzed binding-energy range.

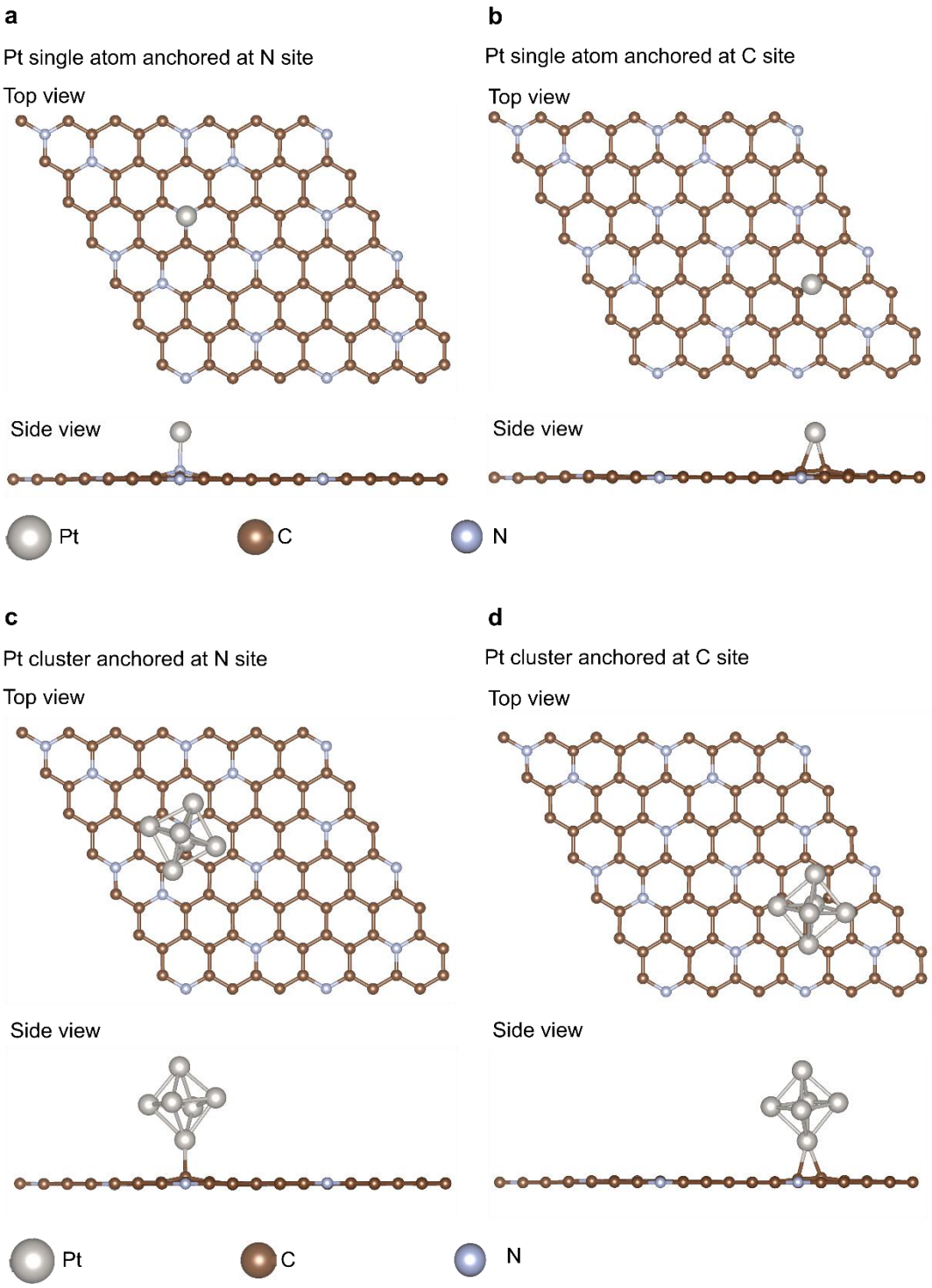

Figure S11. DFT-optimized structural models of isolated Pt atoms and Pt clusters anchored on N-doped graphene. (a, b) Top and side views of an isolated Pt atom anchored at (a) an N site and (b) a C site. (c, d) Top and side views of a Pt cluster anchored at (c) an N site and (d) a C site. Grey, brown, and light blue spheres represent Pt, C, and N atoms, respectively.

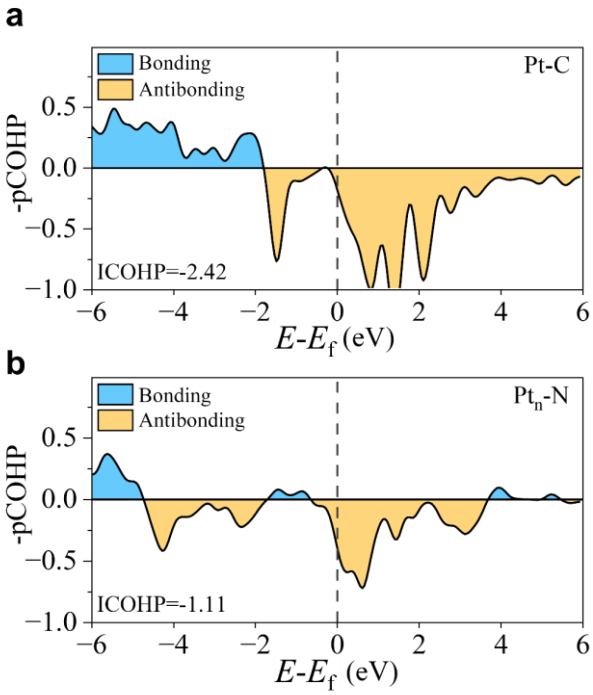

Figure S12. COHP analysis of Pt–C and Pt–N interactions. (a) Pt–C interaction for Pt single atoms. (b) Pt–N interaction for Pt clusters.

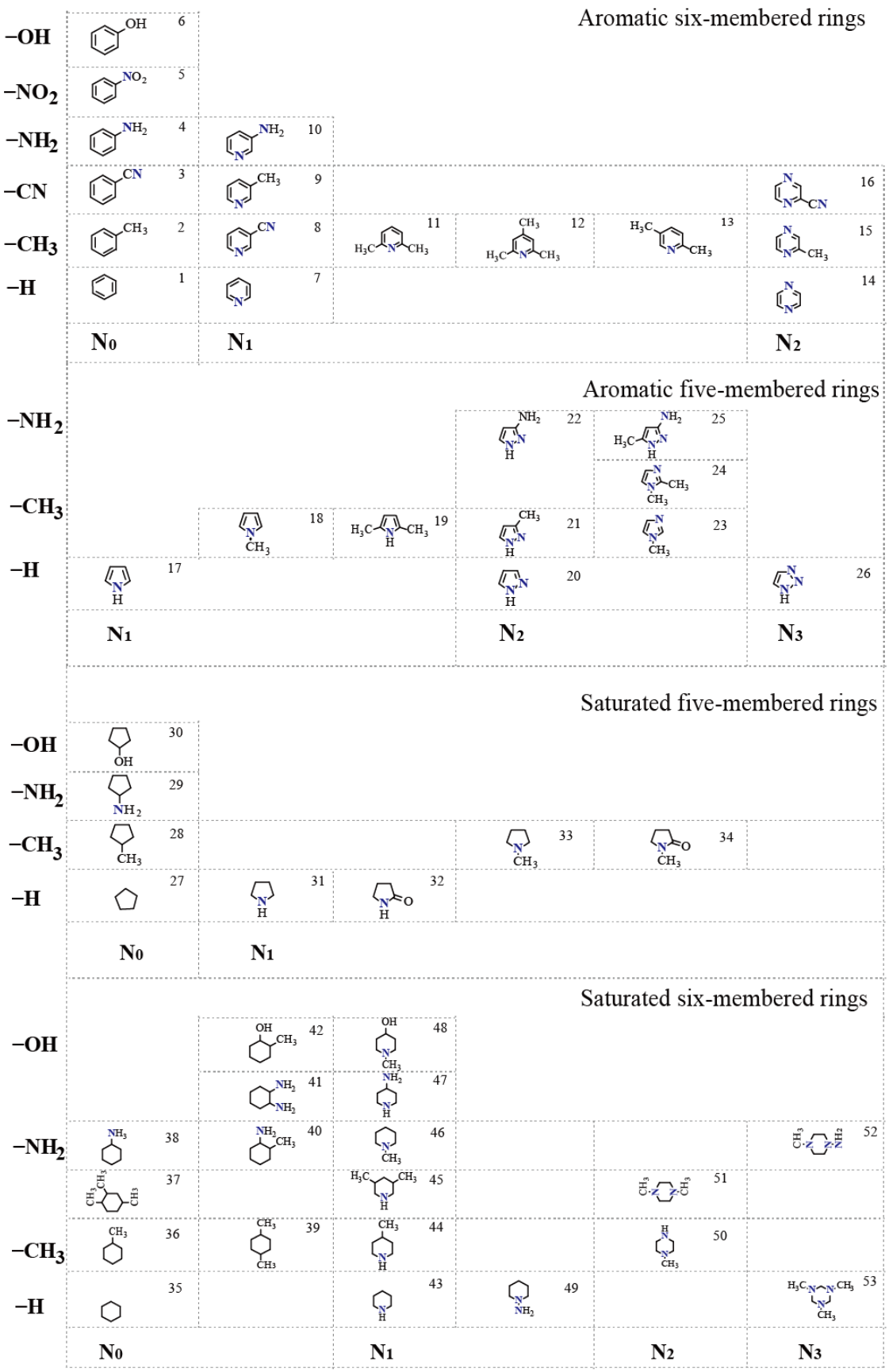

Figure S13. Structural classification of cyclic organic precursors. Precursors are grouped by the number of nitrogen atoms, where N_x denotes x nitrogen atoms in each cyclic molecule.

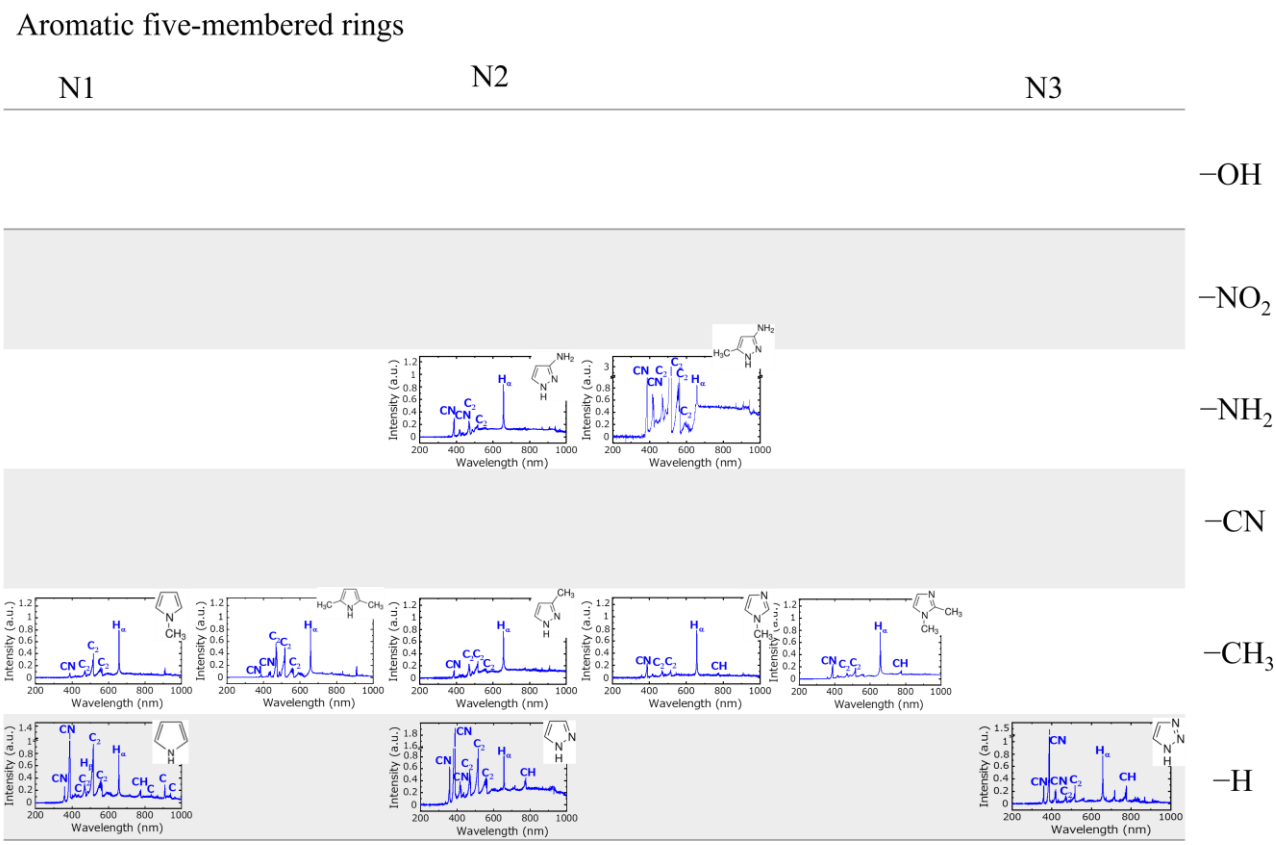

Figure S14. Optical emission spectra of aromatic five-membered-ring precursors. Spectra are grouped according to the substituent on the aromatic ring, with the main plasma-emission species identified.

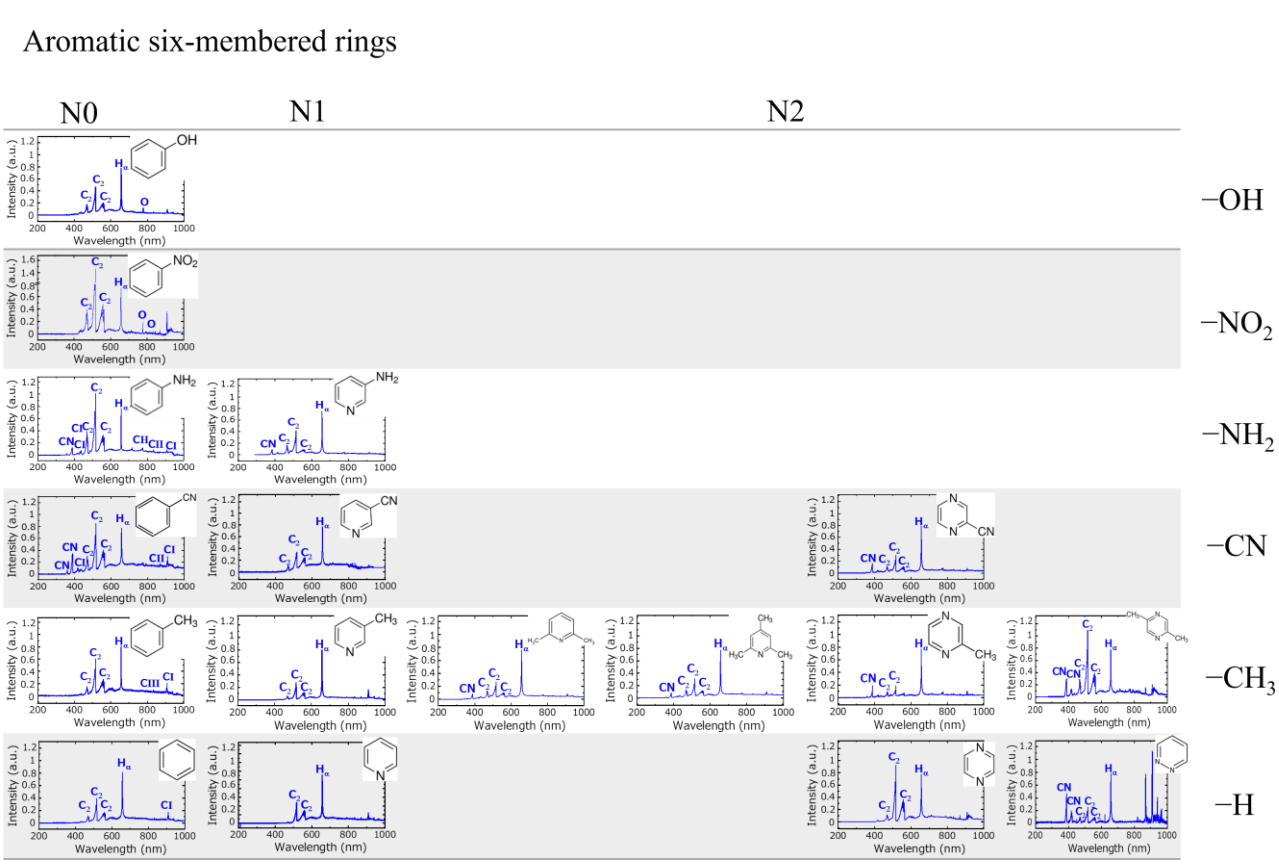

Figure S15. Optical emission spectra of aromatic six-membered-ring precursors. Spectra are grouped according to the substituent on the aromatic ring, with the main plasma-emission species identified.

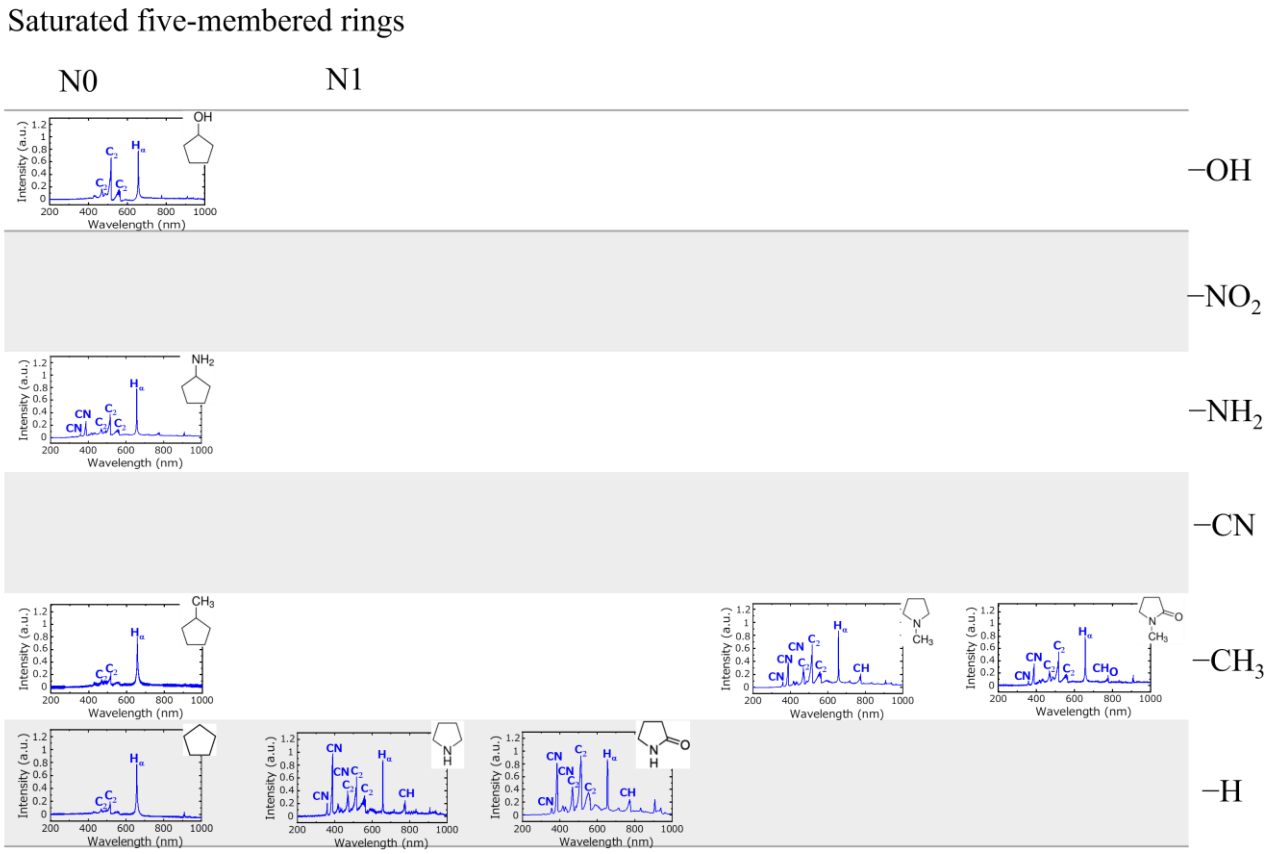

Figure S16. Optical emission spectra of saturated five-membered-ring precursors. Spectra are grouped according to the substituent on the ring, with the main plasma-emission species identified.

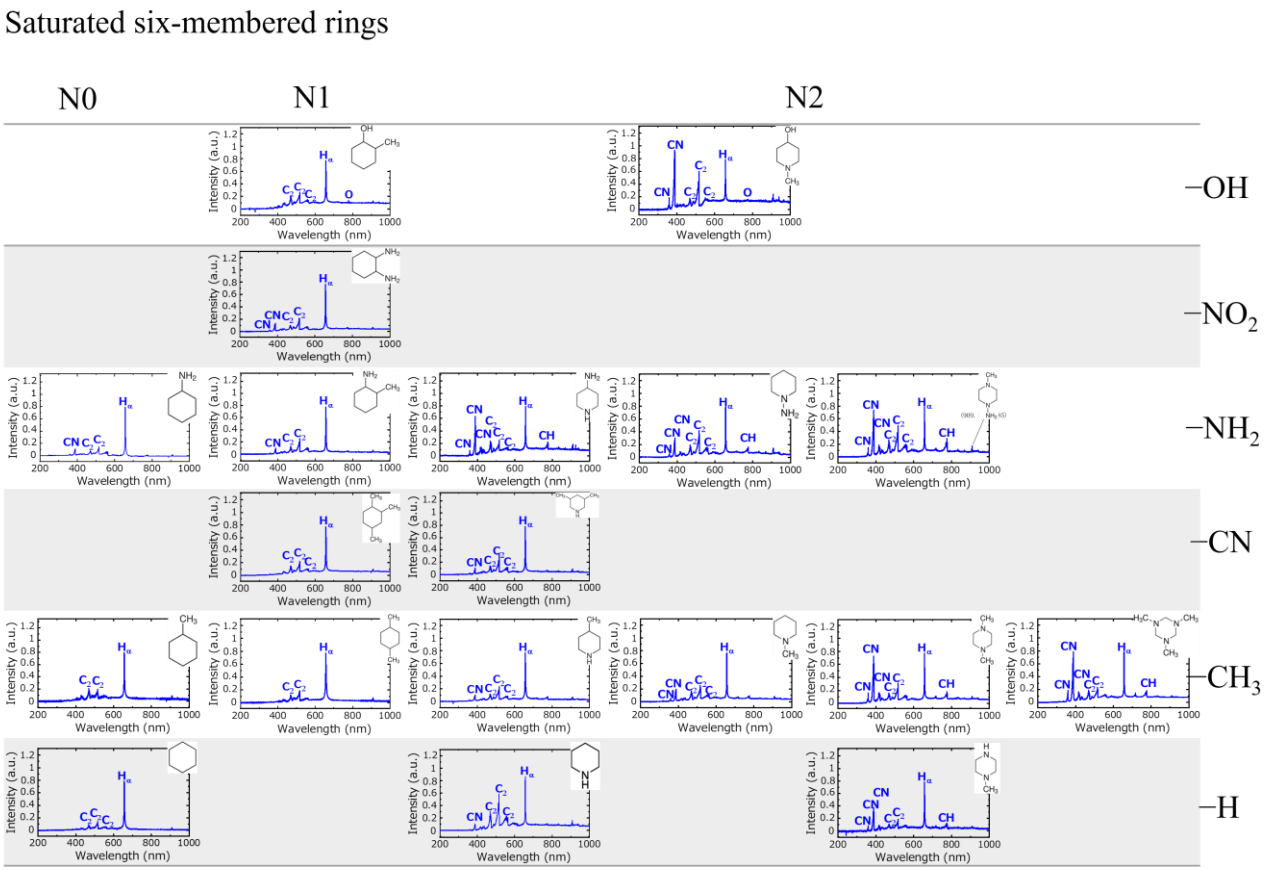

Figure S17. Optical emission spectra of saturated six-membered-ring precursors. Spectra are grouped according to the substituent on the ring, with the main plasma-emission species identified.

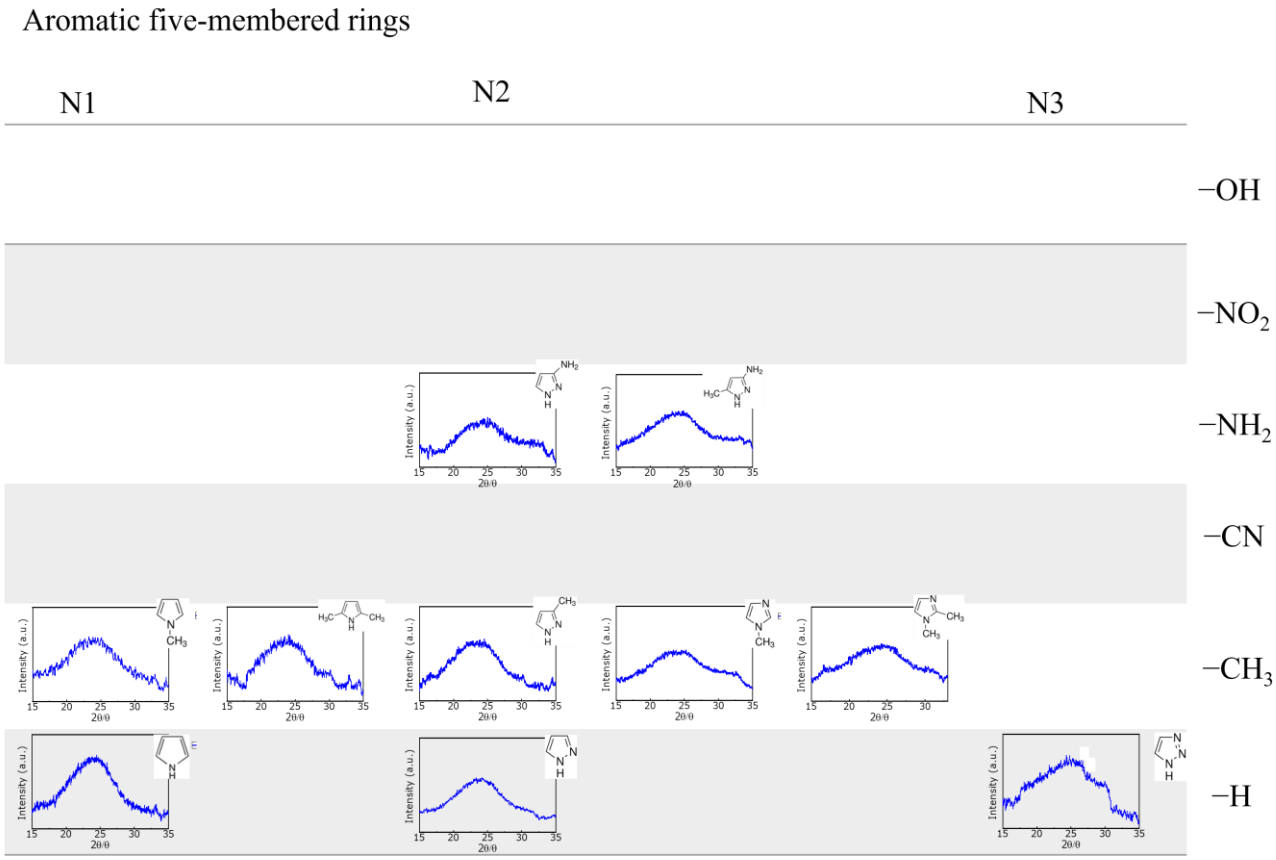

Figure S18. XRD patterns of carbons derived from aromatic five-membered-ring precursors. Patterns are grouped according to the nitrogen content and substituent type of the precursor molecules.

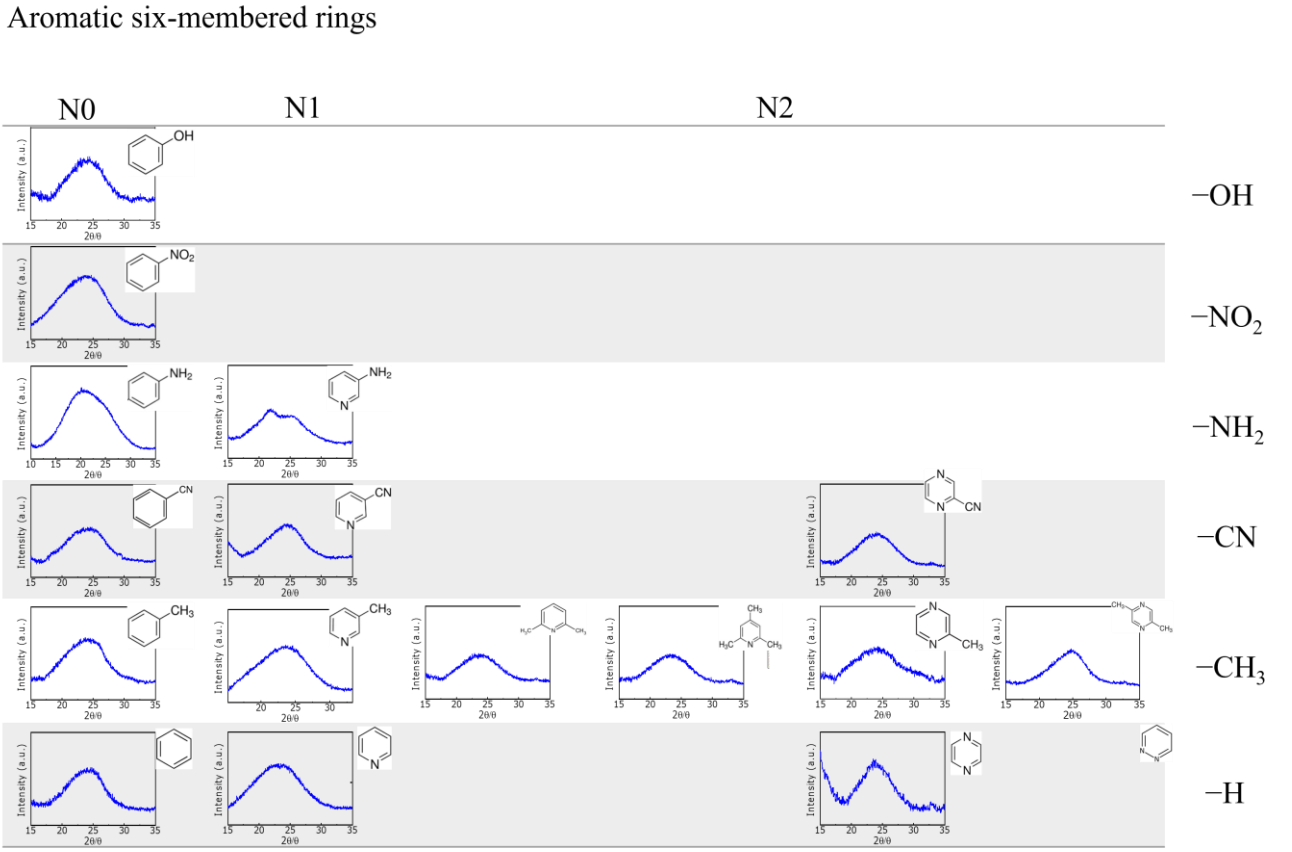

Figure S19. XRD patterns of carbons derived from aromatic six-membered-ring precursors. Patterns are grouped according to the nitrogen content and substituent type of the precursor molecules.

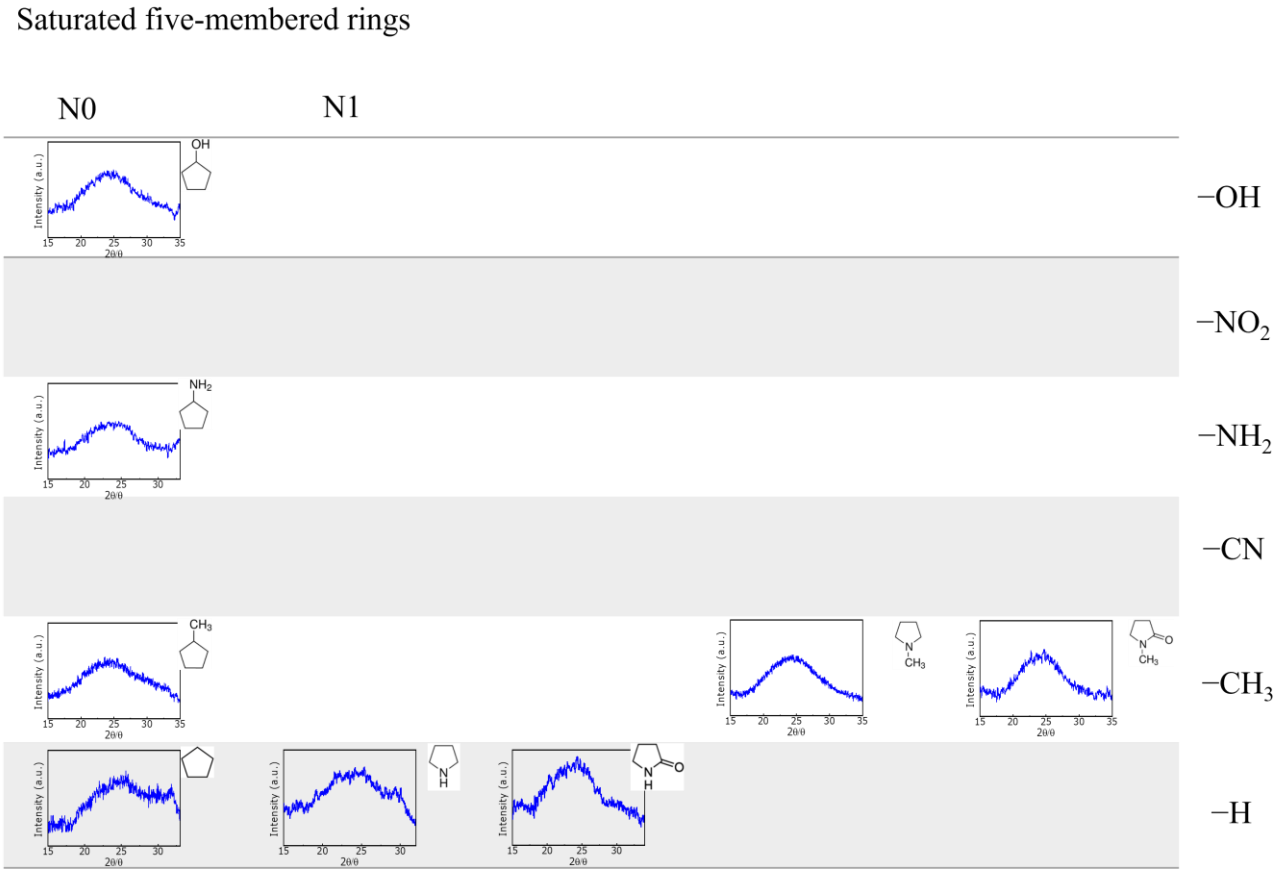

Figure S20. XRD patterns of carbons derived from saturated five-membered-ring precursors. Patterns are grouped according to the nitrogen content and substituent type of the precursor molecules.

Saturated six-membered rings

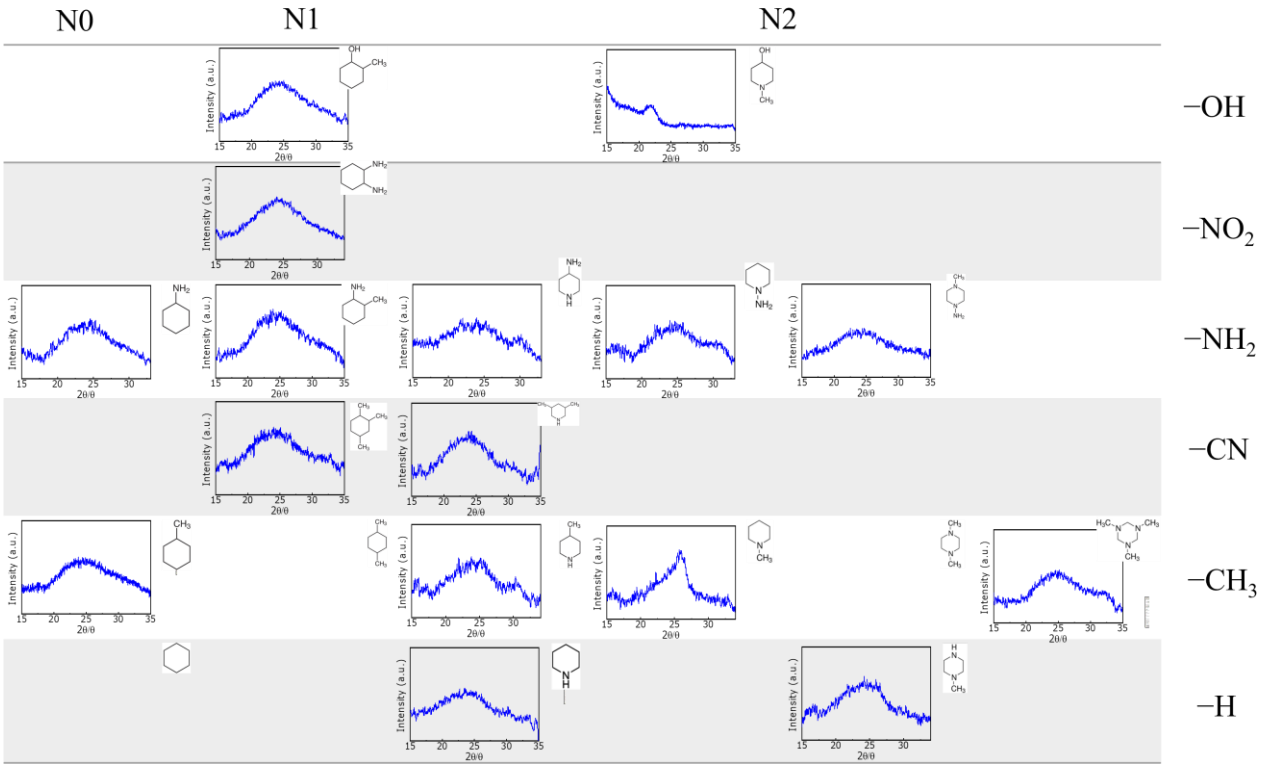

Figure S21. XRD patterns of carbons derived from saturated six-membered-ring precursors. Patterns are grouped according to the nitrogen content and substituent type of the precursor molecules.

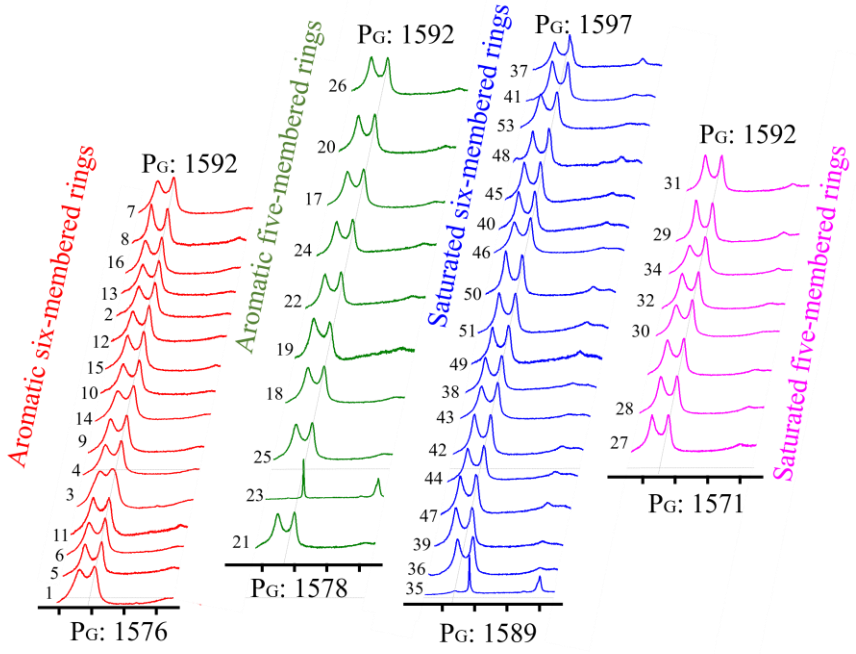

Figure S22. Raman spectra of solution-plasma-derived carbons. Spectra are grouped by precursor ring type, with the corresponding G-band peak positions indicated.

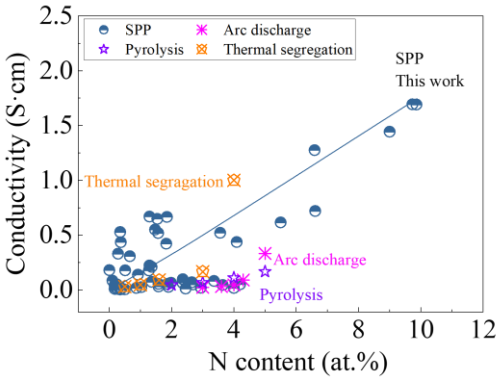

Figure S23. Electrical conductivity versus nitrogen content in carbon materials. Comparison of solution-plasma-derived carbons with those produced by arc discharge, thermal segregation, and pyrolysis.

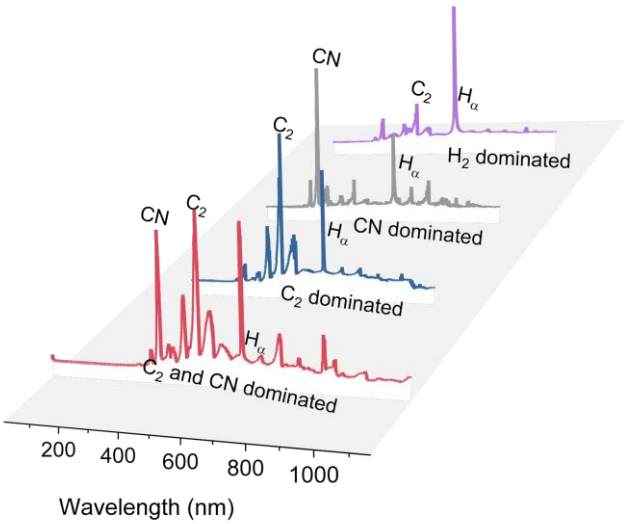

Figure S24. Representative OES patterns of dominant reactive species. Spectra are classified as C_2+CN, C_2, H, and CN dominated spectra.

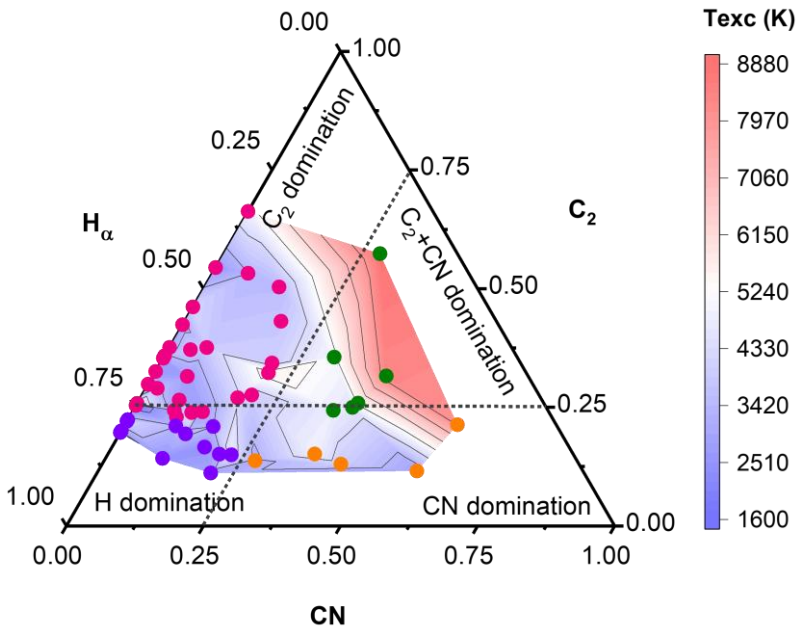

Figure S25. Excitation temperature distribution across OES patterns. Ternary correlation of H_α, C_2, and CN emission contributions with excitation temperature calculated from Balmer H lines.

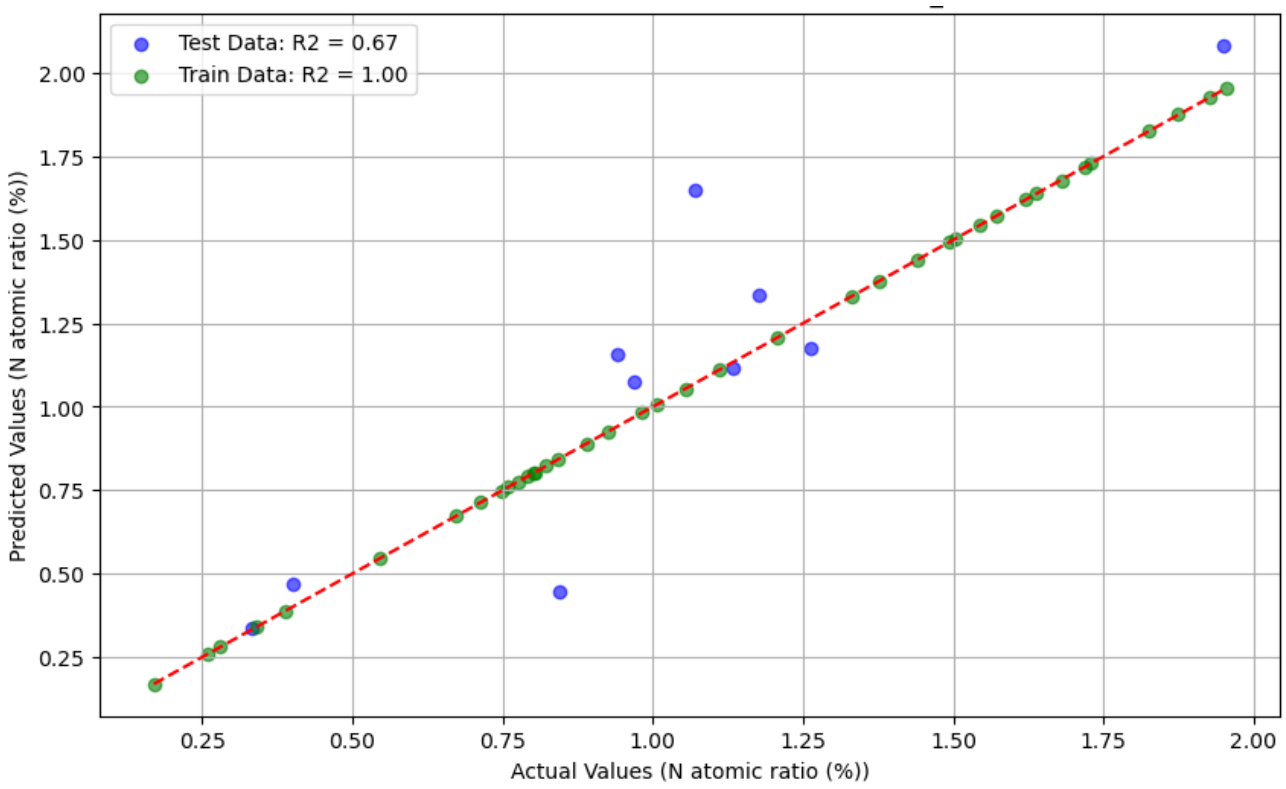

Figure S26. Validation of the MLP model for predicting nitrogen content. Comparison between predicted and observed nitrogen contents for training and test datasets, with corresponding R^2 values indicated.

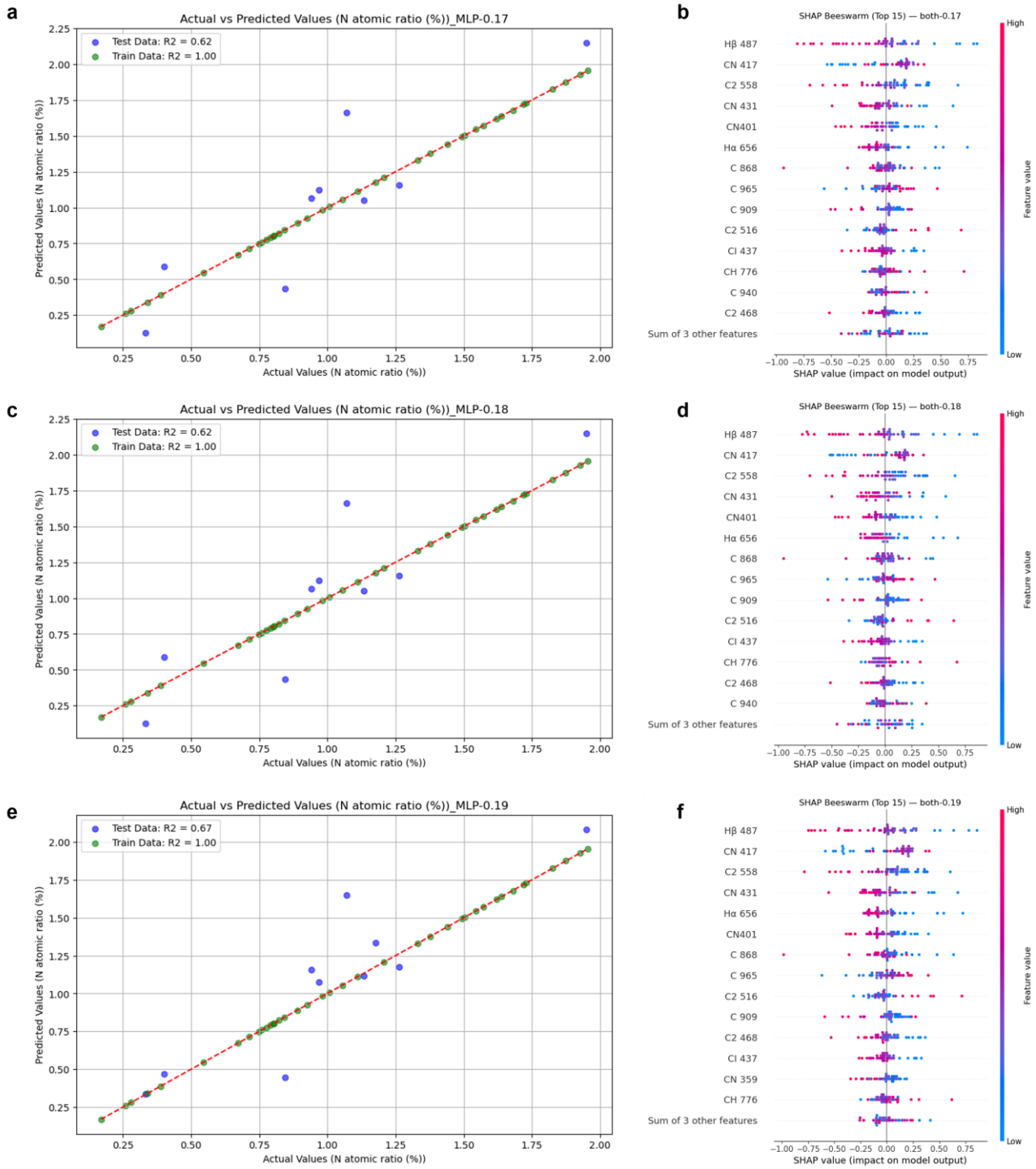

Figure S27. Validation of the MLP model for predicting nitrogen content and SHAP analysis corresponding to various train/test split ratios. (a, c, e) Comparison between actual and predicted N atomic ratios for the training and test datasets using train/test split ratios of 83/17, 82/18, and 81/19, respectively. The corresponding R^2 values are shown in each panel. (b, d, f) SHAP beeswarm plots showing the top spectral features contributing to the MLP predictions under the same split ratios. The feature color represents the relative feature value.

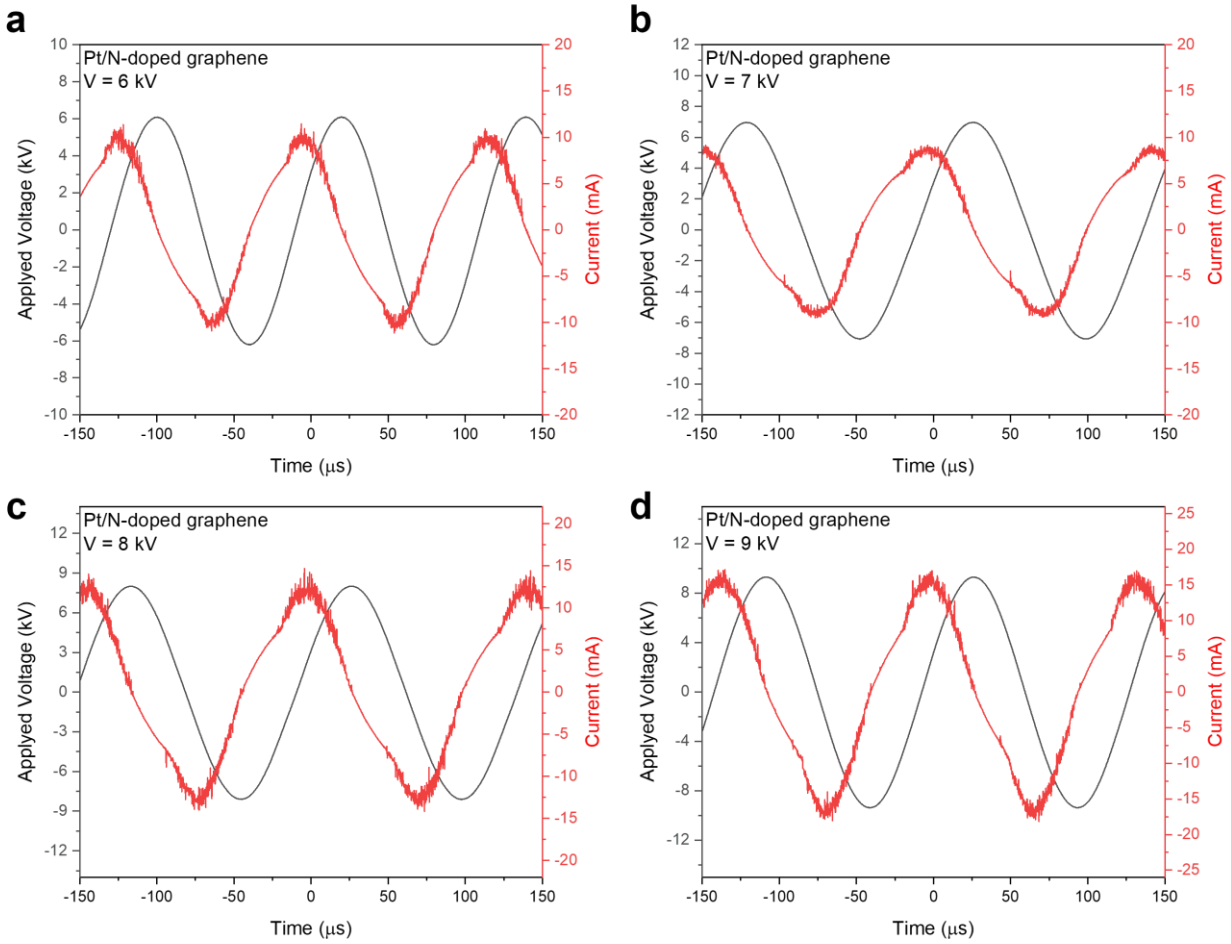

Figure S28. Voltage and current waveforms recorded during plasma-catalytic NH_3 synthesis catalyzed by Pt/N-doped graphene. (a) 6 kV, (b) 7 kV, (c) 8 kV, and (d) 9 kV.

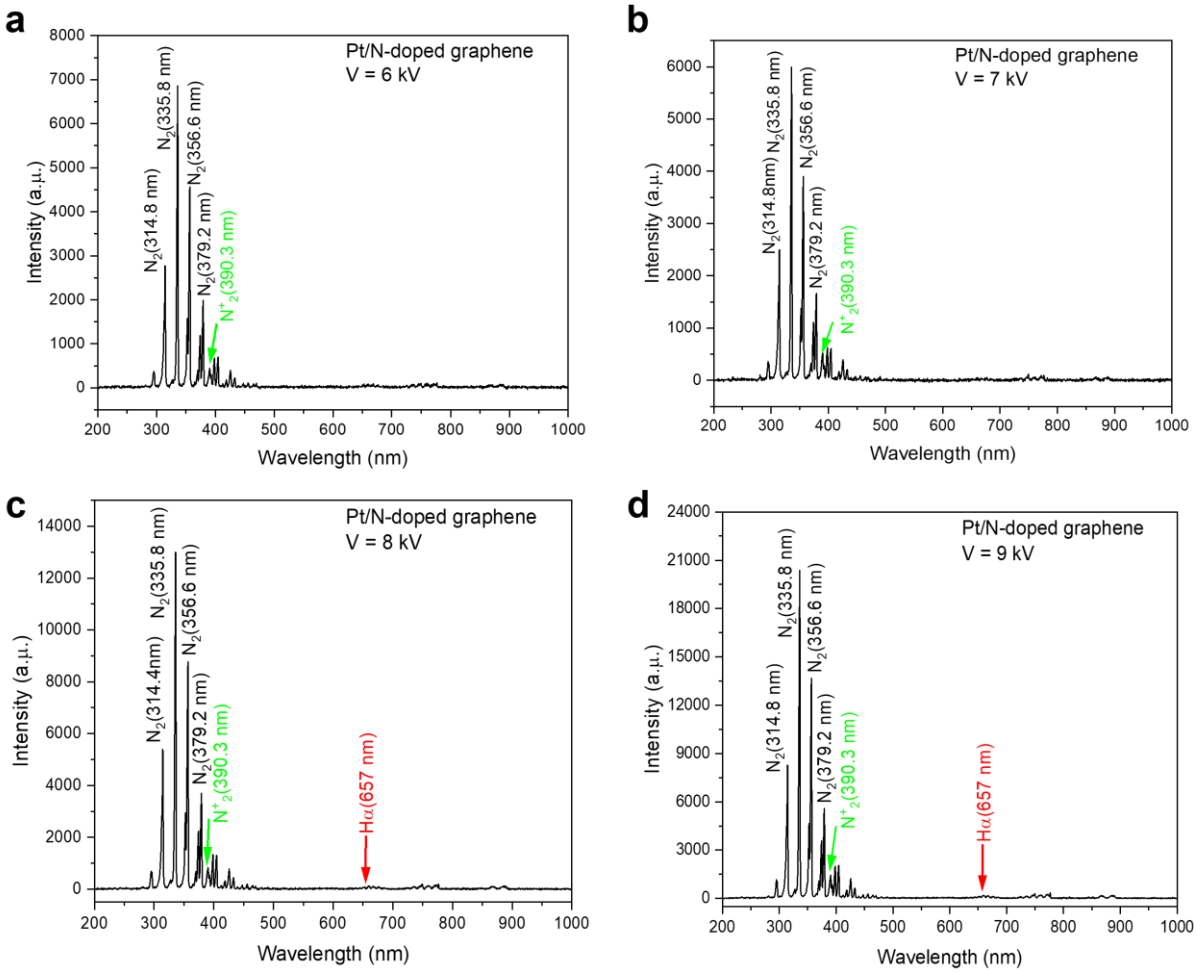

Figure S29. Optical emission spectra recorded during plasma-catalytic NH_3 synthesis catalyzed by Pt/N-doped graphene. (a) 6 kV, (b) 7 kV, (c) 8 kV, and (d) 9 kV.

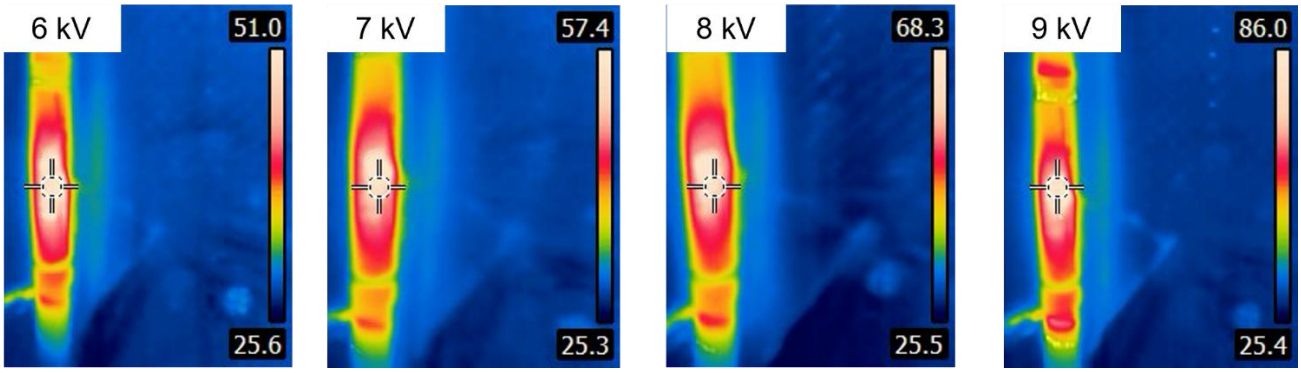

Figure S30. Infrared thermal images recorded during plasma-catalytic NH_3 synthesis catalyzed by Pt/N-doped graphene. The temperature scale bars on the right of each figure indicate the minimum and maximum temperatures within the selected imaging region at applied voltages of 6, 7, 8, and 9 kV.

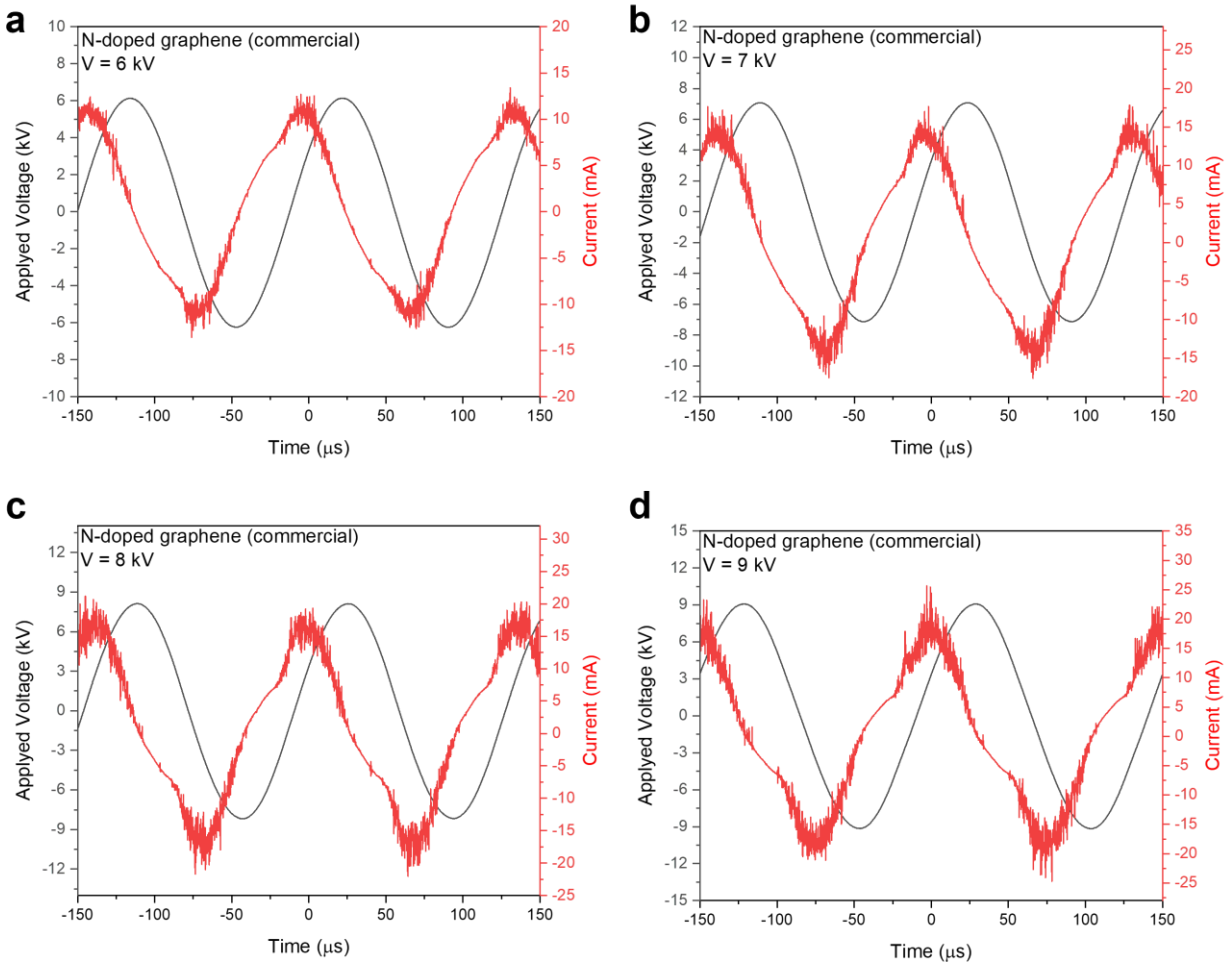

Figure S31. Voltage and current waveforms recorded during plasma-catalytic NH_3 synthesis catalyzed by commercial N-doped graphene. (a) 6 kV, (b) 7 kV, (c) 8 kV, and (d) 9 kV.

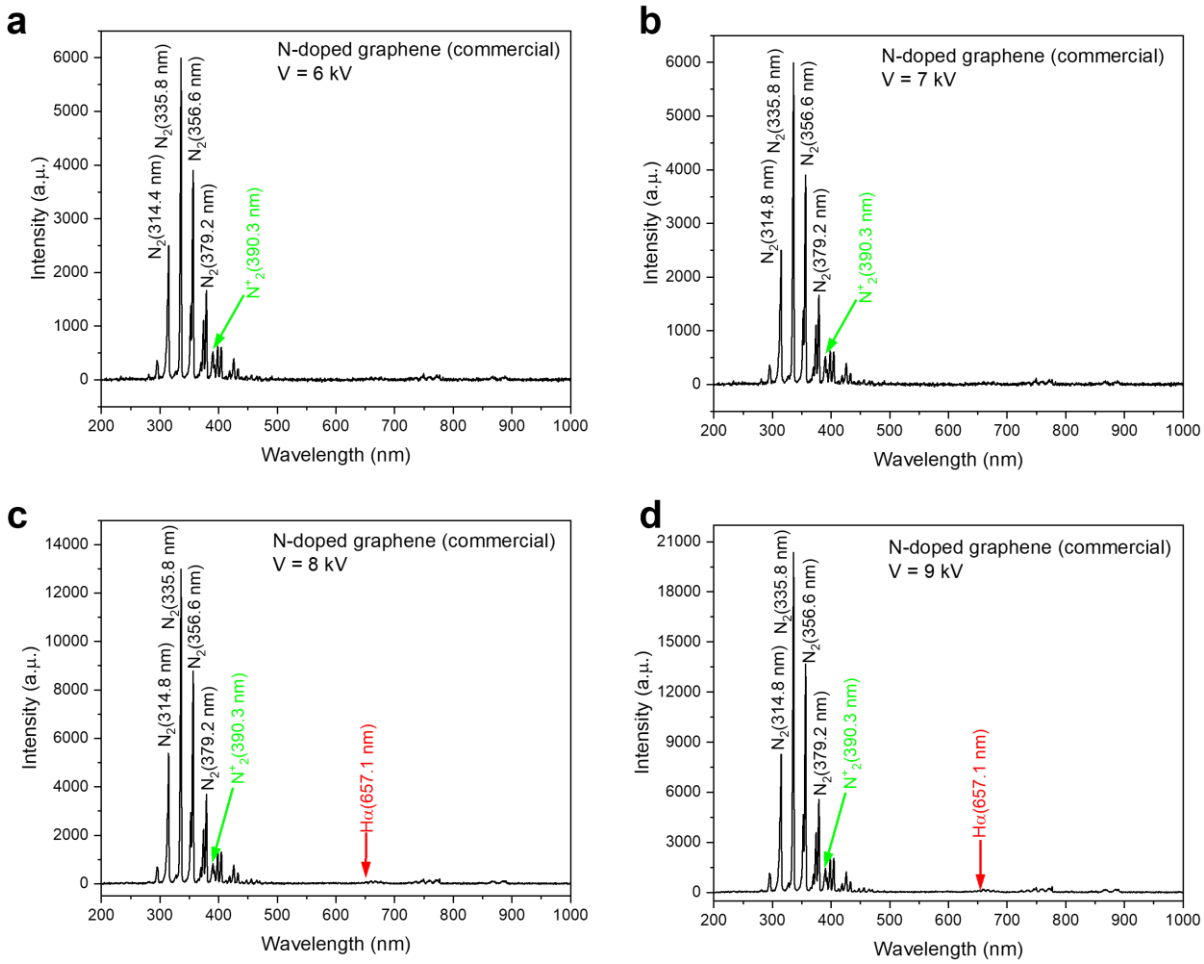

Figure S32. Optical emission spectra recorded during plasma-catalytic NH_3 synthesis catalyzed by commercial N-doped graphene. (a) 6 kV, (b) 7 kV, (c) 8 kV, and (d) 9 kV.

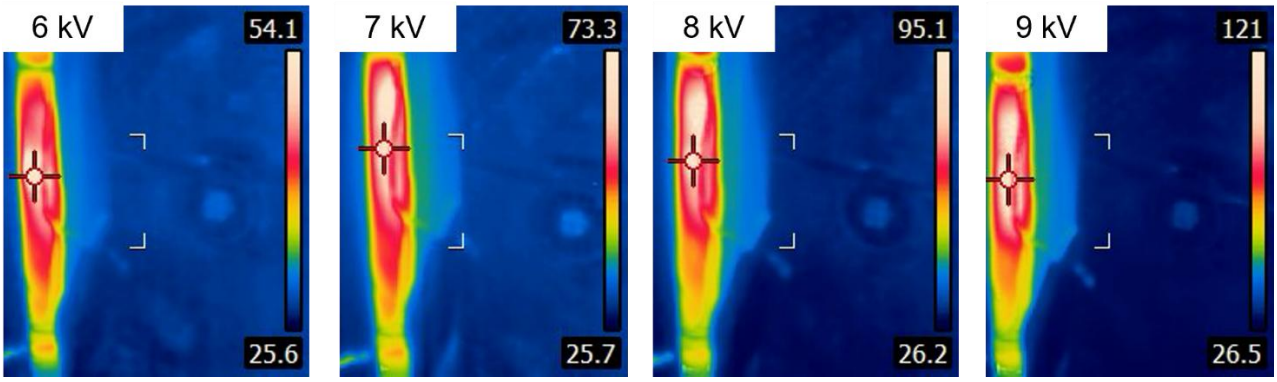

Figure S33. Infrared thermal images recorded during plasma-catalytic NH_3 synthesis catalyzed by commercial N-doped graphene. The temperature scale bars on the right of each figure indicate the minimum and maximum temperatures within the selected imaging region at applied voltages of 6, 7, 8, and 9 kV.

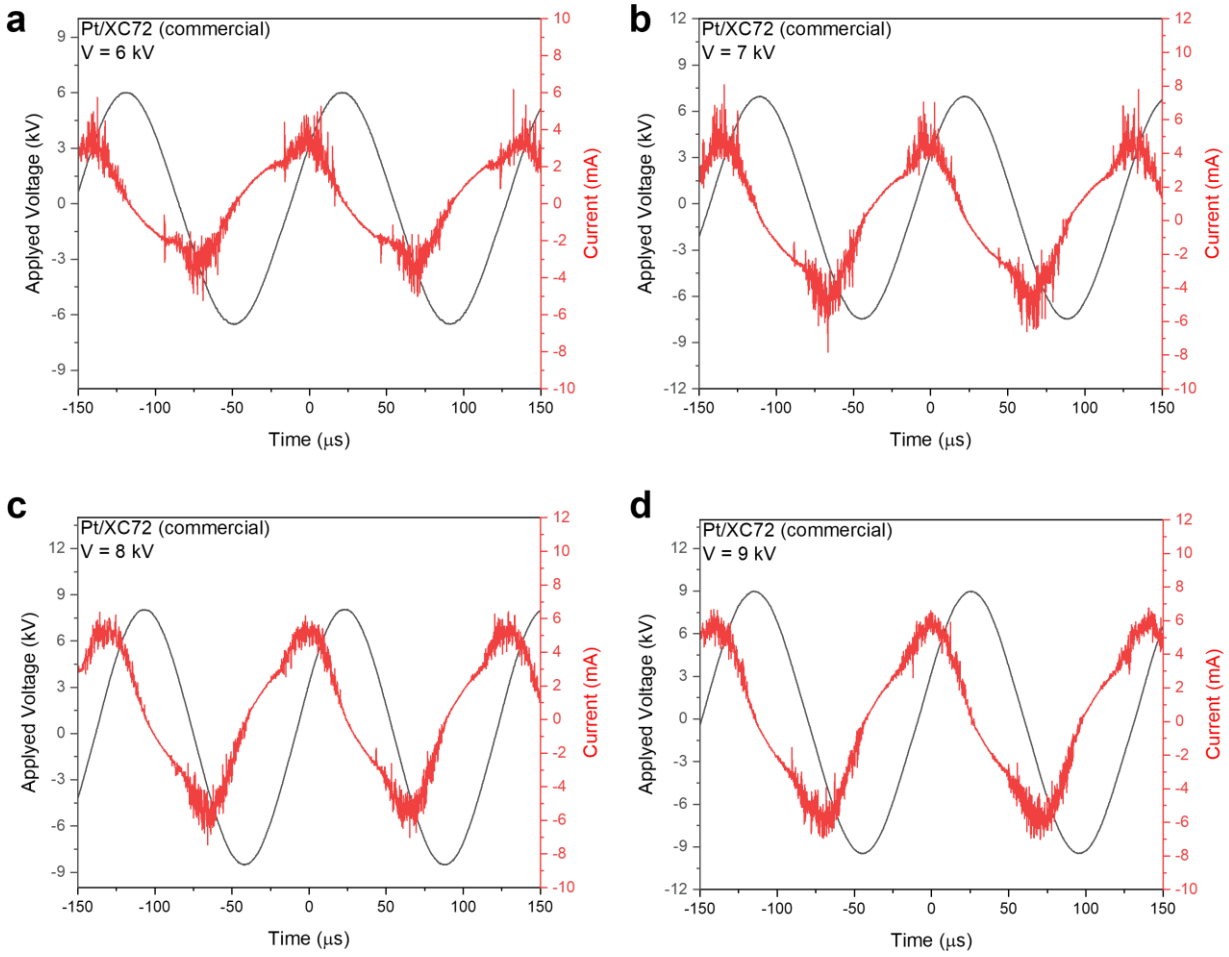

Figure S34. Voltage and current waveforms recorded during plasma-catalytic NH_3 synthesis catalyzed by Pt/XC72. (a) 6 kV, (b) 7 kV, (c) 8 kV, and (d) 9 kV.

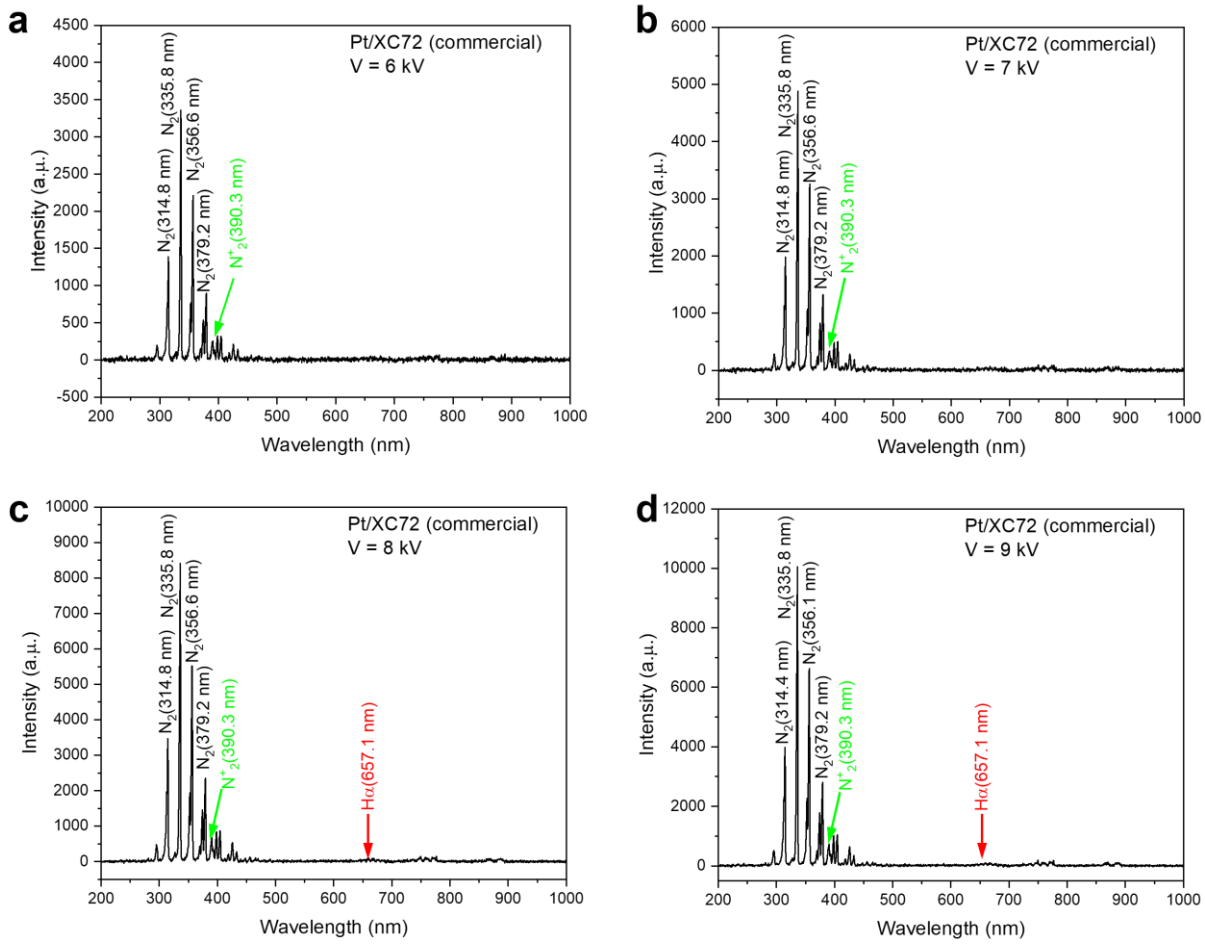

Figure S35. Optical emission spectra recorded during plasma-catalytic NH_3 synthesis catalyzed by Pt/XC72. (a) 6 kV, (b) 7 kV, (c) 8 kV, and (d) 9 kV.

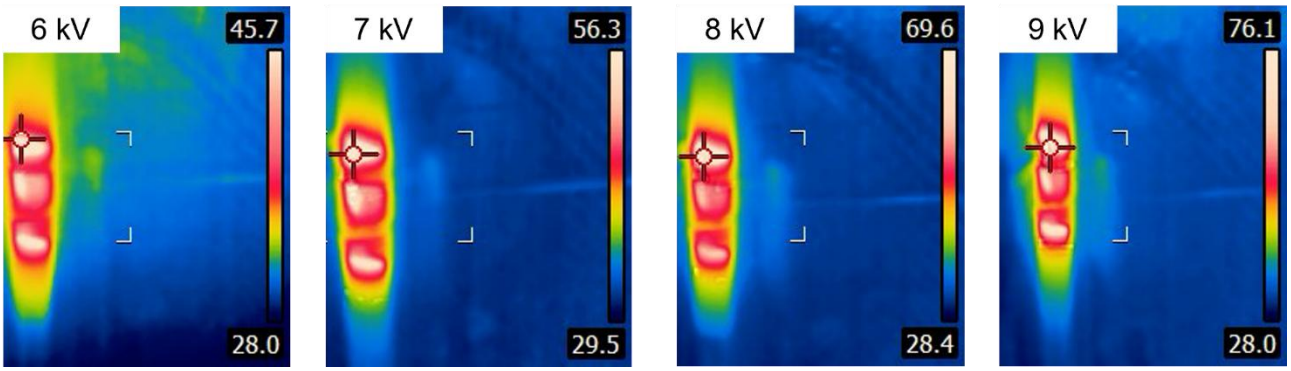

Figure S36. Infrared thermal images recorded during plasma-catalytic NH_3 synthesis catalyzed by Pt/XC72. The temperature scale bars on the right of each figure indicate the minimum and maximum temperatures within the selected imaging region at applied voltages of 6, 7, 8, and 9 kV.

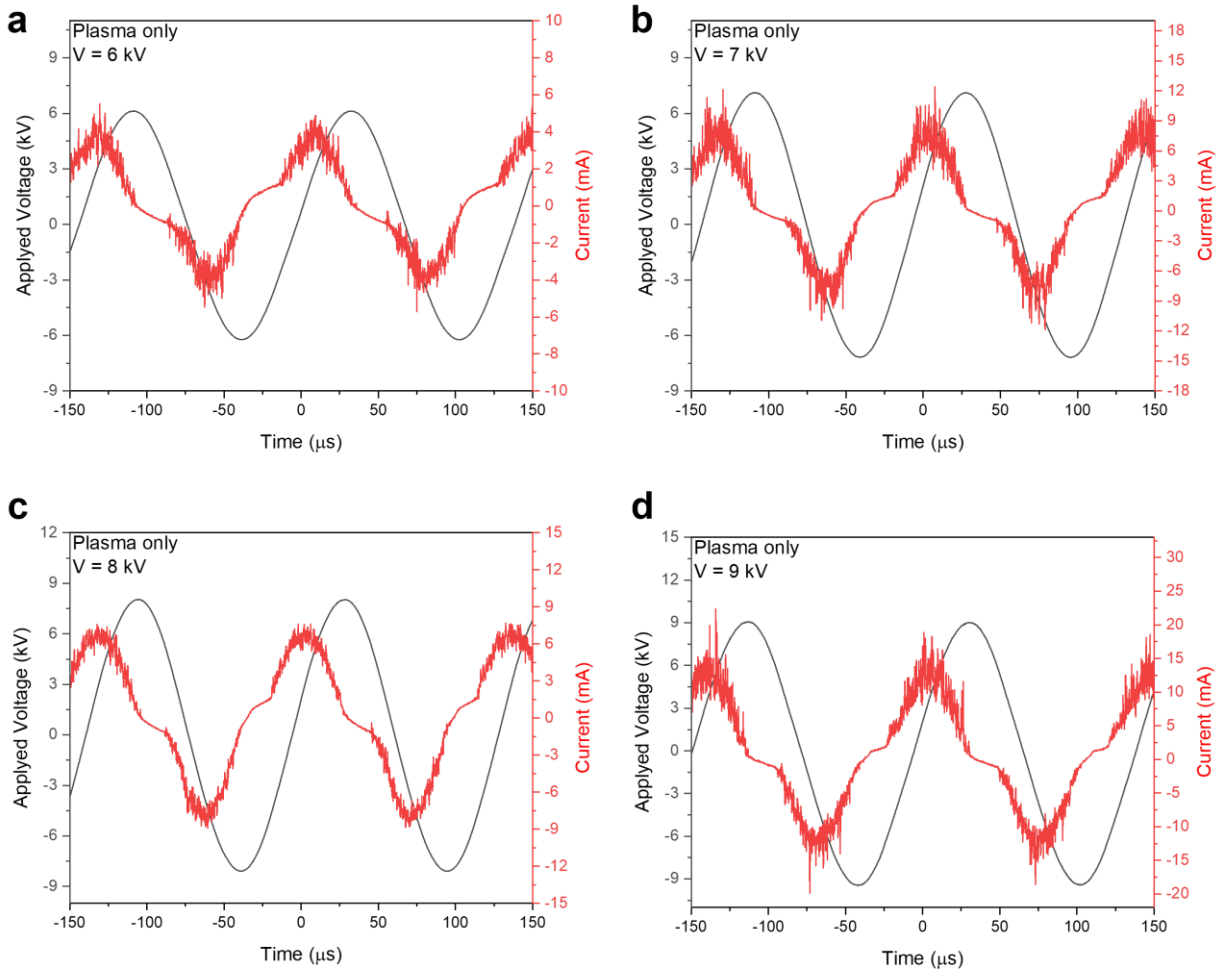

Figure S37. Voltage and current waveforms recorded during plasma-catalytic NH_3 synthesis catalyzed by plasma-only conditions. (a) 6 kV, (b) 7 kV, (c) 8 kV, and (d) 9 kV.

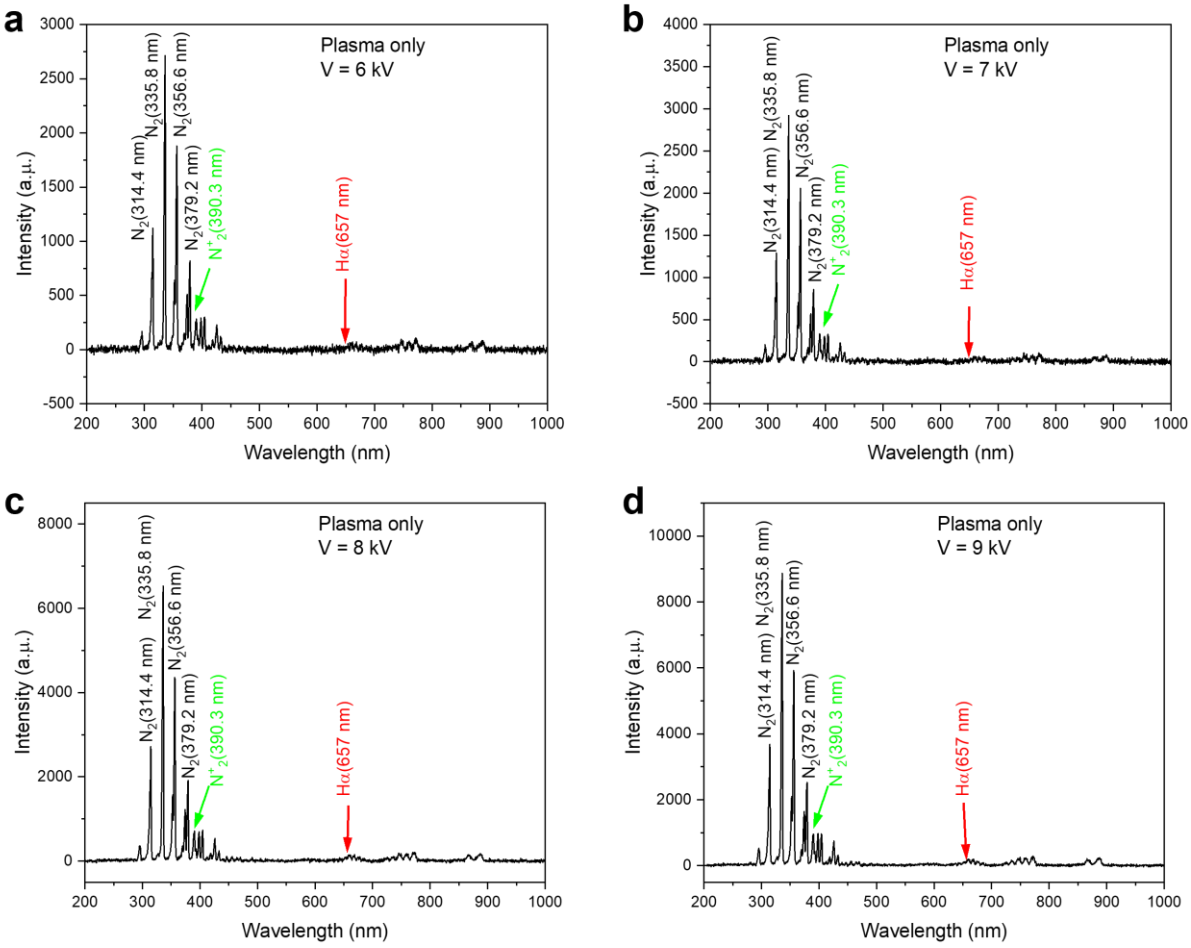

Figure S38. Optical emission spectra recorded during plasma-catalytic NH_3 synthesis catalyzed by plasma-only conditions. (a) 6 kV, (b) 7 kV, (c) 8 kV, and (d) 9 kV.

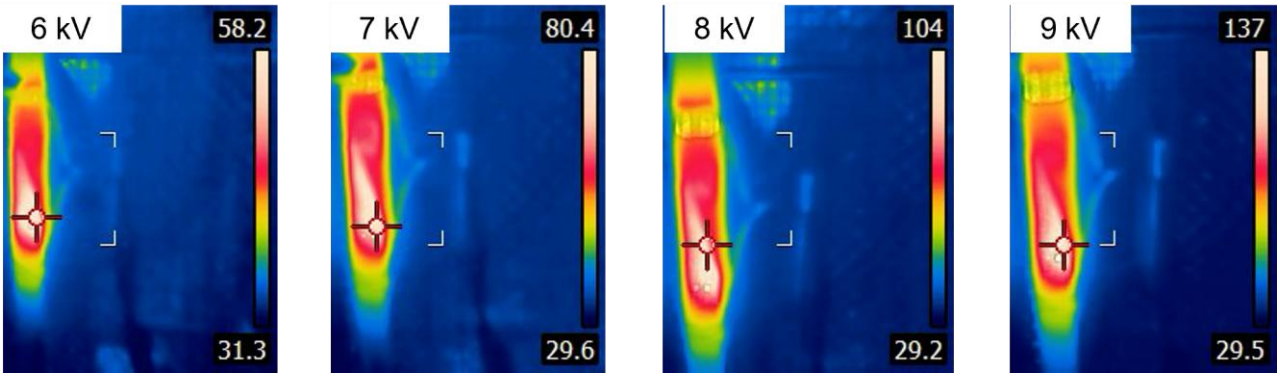

Figure S39. Infrared thermal images recorded during plasma-catalytic NH_3 synthesis catalyzed by plasma-only conditions. The temperature scale bars on the right of each figure indicate the minimum and maximum temperatures within the selected imaging region at applied voltages of 6, 7, 8, and 9 kV.

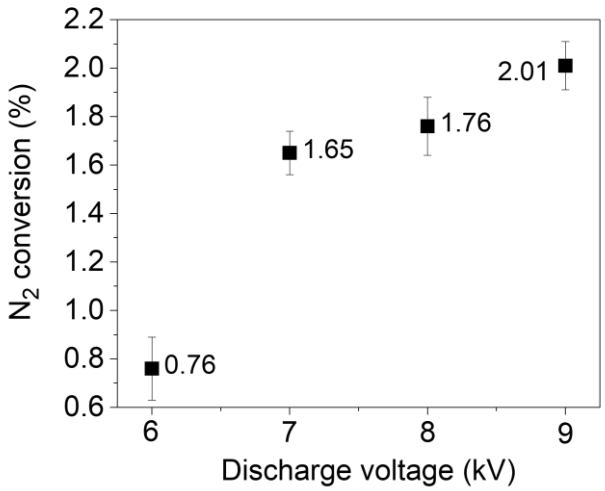

Figure S40. Effect of discharge voltage on N_2 conversion. N_2 conversion over Pt-supported N-doped carbon in a flow reactor at discharge voltages of 6–9 kV.

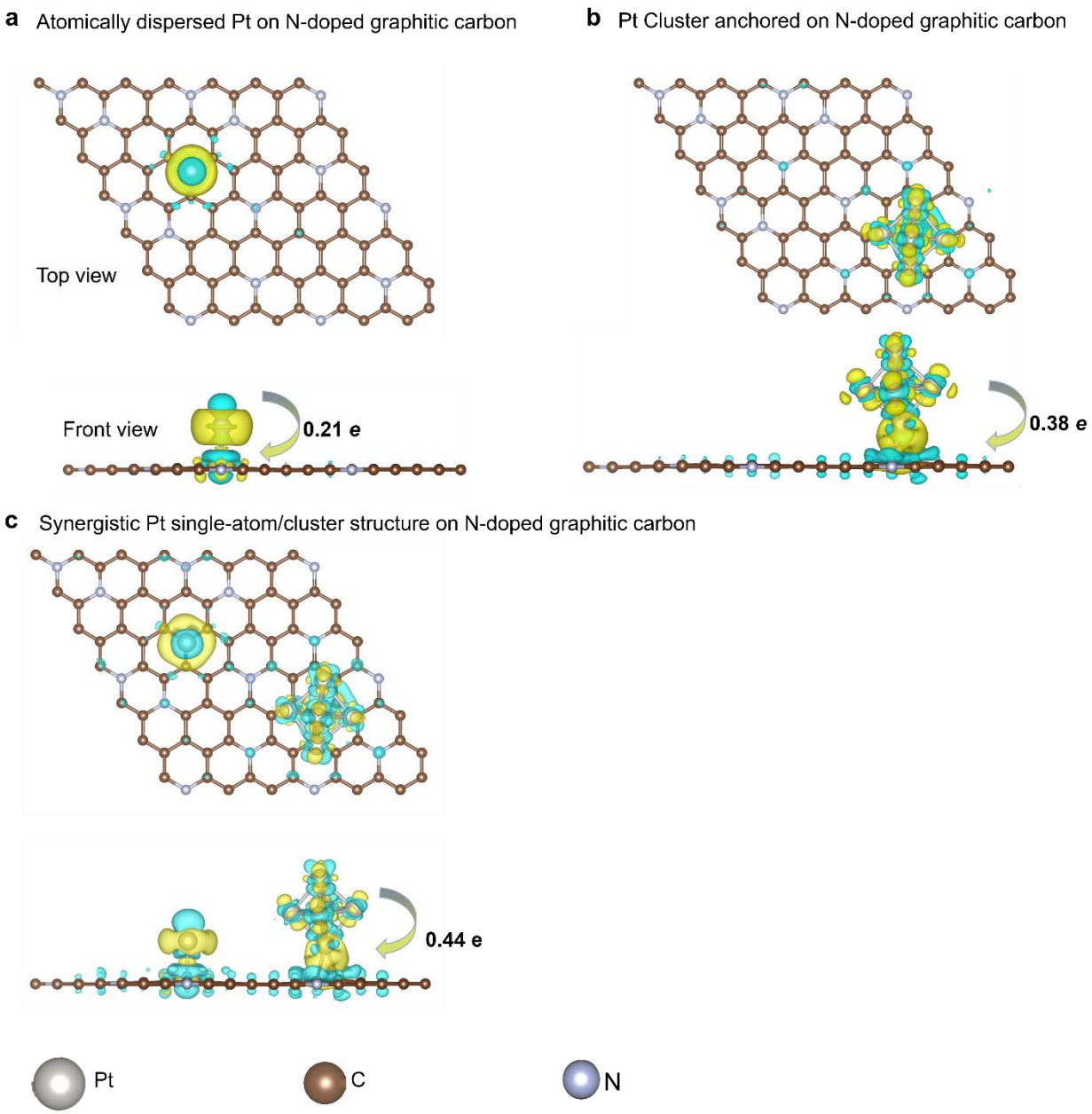

Figure S41. Differential charge density of Pt single-atom and cluster configurations on N-doped graphitic carbon. (a–c) Pt single atom, Pt cluster, and coupled Pt single-atom/Pt-cluster configurations, respectively. Yellow and cyan regions denote electron accumulation and depletion. The corresponding electron transfers from Pt to the N-doped carbon support are 0.21, 0.38, and 0.44 e, respectively. Grey, brown, and light-blue spheres represent Pt, C, and N atoms.

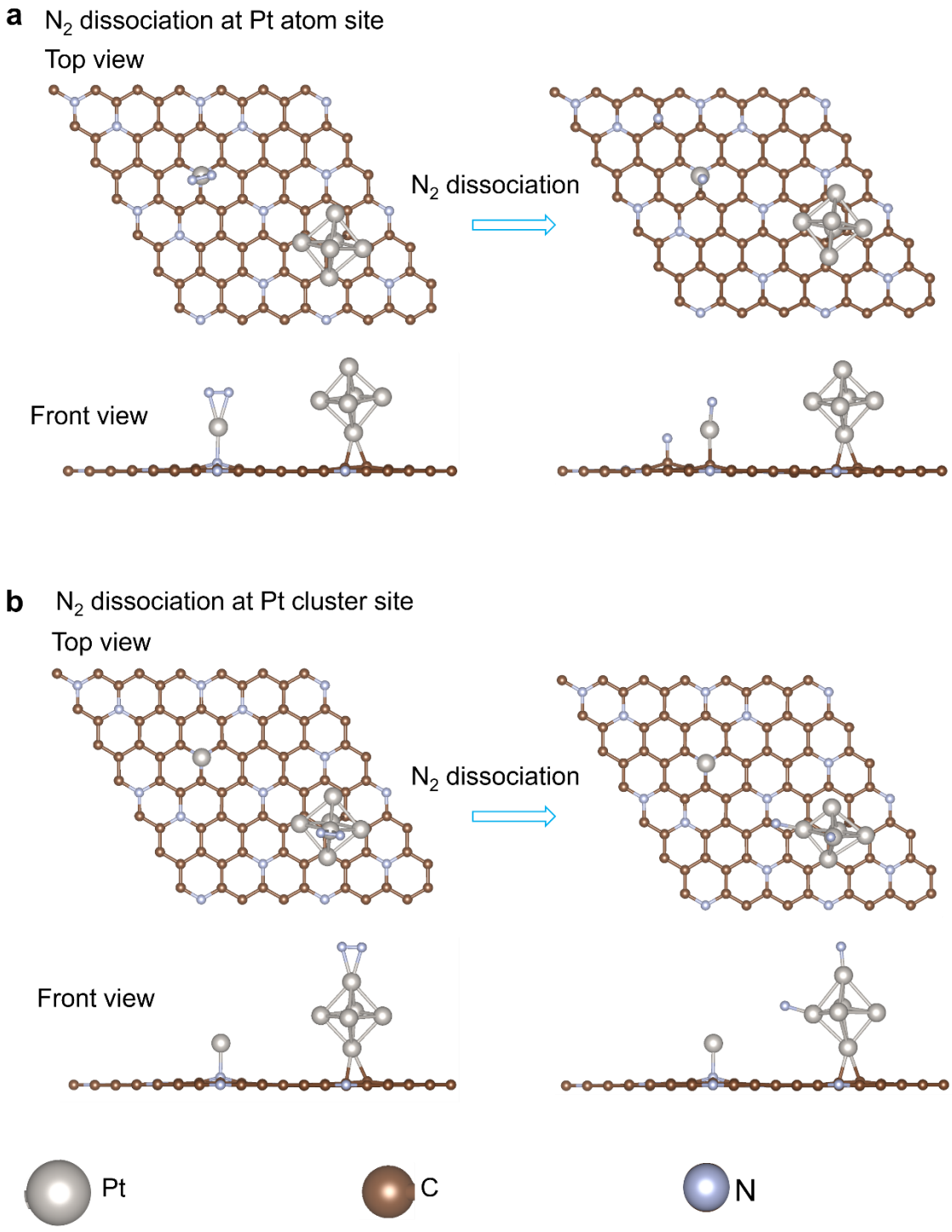

Figure S42. Optimized structures for N_2 dissociation on Pt sites anchored on N-doped graphitic carbon. (a) Initial and final configurations for N_2 dissociation on an atomically dispersed Pt site. (b) Initial and final configurations for N_2 dissociation on a Pt cluster site.

Top and front views are shown for each configuration. Grey, brown, and light blue spheres represent Pt, C, and N atoms, respectively.

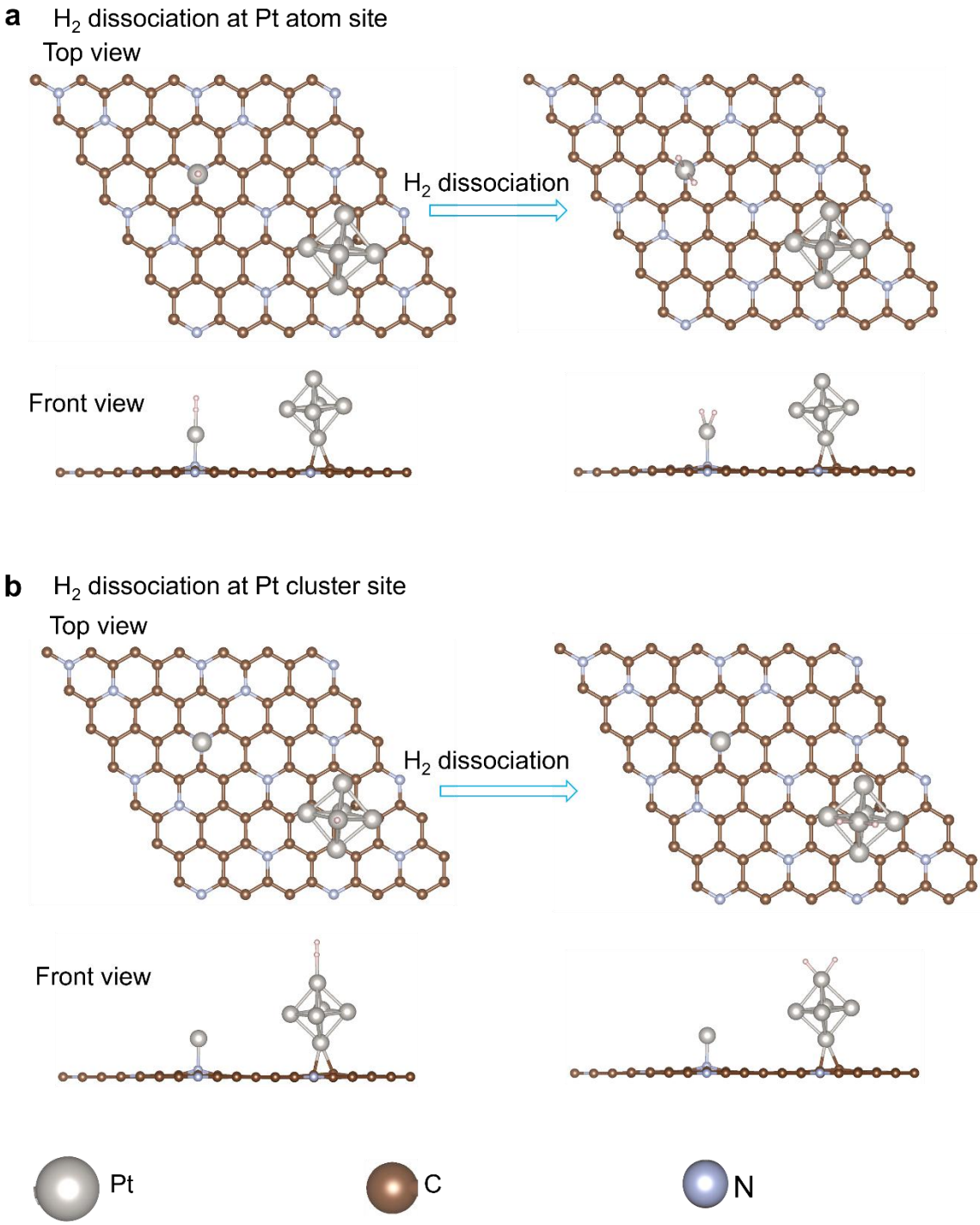

Figure S43. Optimized structures for H_2 dissociation on Pt sites anchored on N-doped graphitic carbon. (a) Initial and final configurations for H_2 dissociation on an atomically dispersed Pt site. (b) Initial and final configurations for H_2 dissociation on a Pt cluster site.

Top and front views are shown for each configuration. Grey, brown, and light blue spheres represent Pt, C, and N atoms, respectively.

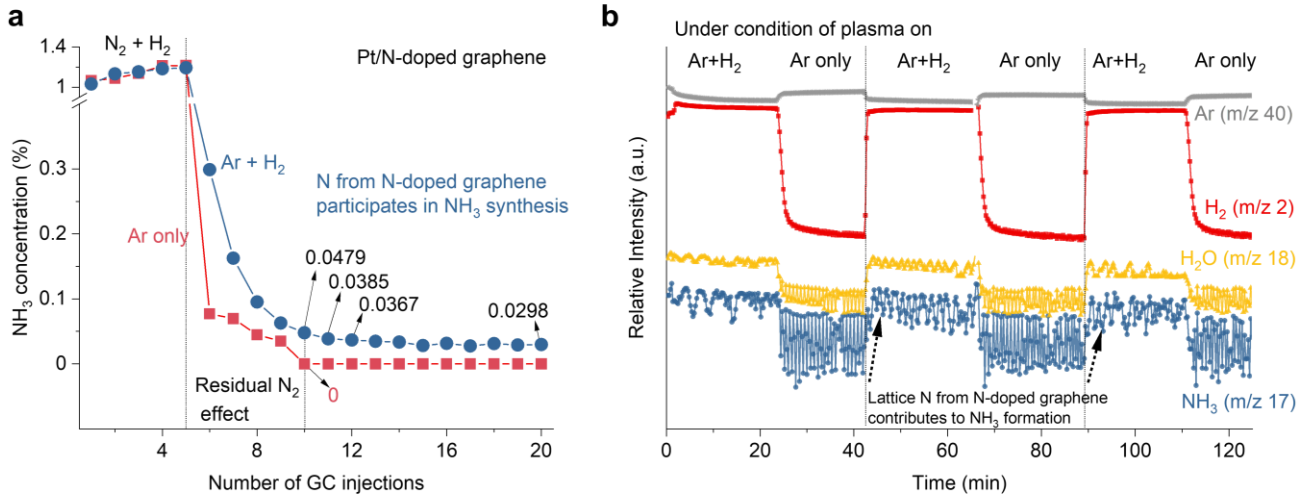

Figure S44.Evidence for lattice-N participation in plasma-catalytic NH_3 synthesis. (a) NH_3 concentration over Pt/N-doped graphene as a function of GC injection number under $N_2 + H_2$, Ar-only, and Ar + H_2 plasma conditions. After switching from $N_2 + H_2$ to Ar-only plasma, the NH_3 signal rapidly decreased. A small residual NH_3 signal under Ar + H_2, in the absence of external N_2, and its gradual decline with successive injections indicate consumption of reactive lattice N species. For these measurements, 240 mg of Pt/N-doped graphene mixed with quartz sand was reduced in H_2/Ar = 2/3 (50 mL(NTP) min^{-1}, 30 min), followed by N_2/H_2 = 1/1 (20 mL(NTP) min^{-1}) plasma treatment at 11.1 kV and 8 kHz. After five GC injections, the feed was switched to H_2/Ar = 1/1 or pure Ar (20 mL(NTP) min^{-1}) for 15 further injections.

(b) Time-resolved online mass spectrometry signals during cyclic switching between Ar/H_2 = 1/1 and pure Ar under continuous plasma operation. NH_3 (*m/z* = 17) increased upon H_2 introduction and decreased under Ar-only conditions, supporting lattice-N participation through a Mars–van Krevelen-type pathway. H_2 (*m/z* = 2) and Ar/H_2O-related signals are shown for comparison. Each feed segment was maintained for 20 min over three switching cycles.

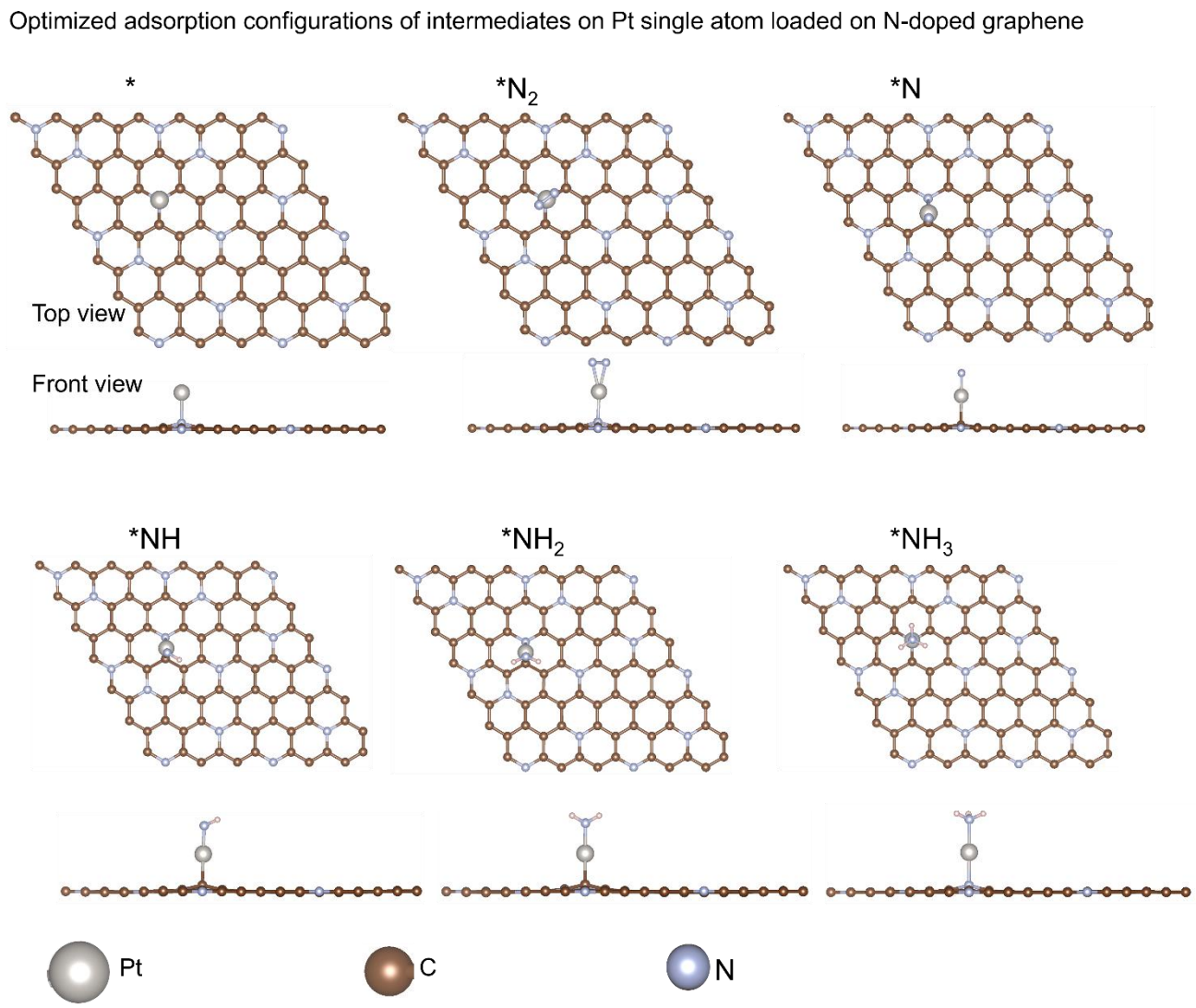

Figure S45. Optimized adsorption configurations of nitrogen-containing intermediates on an atomically dispersed Pt site. Optimized structures of *, *N_2, *N, *NH, *NH_2, and *NH_3 intermediates on an atomically dispersed Pt site anchored on N-doped graphitic carbon. Top and front views are shown for each intermediate. Grey, brown, and light blue spheres represent Pt, C, and N atoms, respectively.

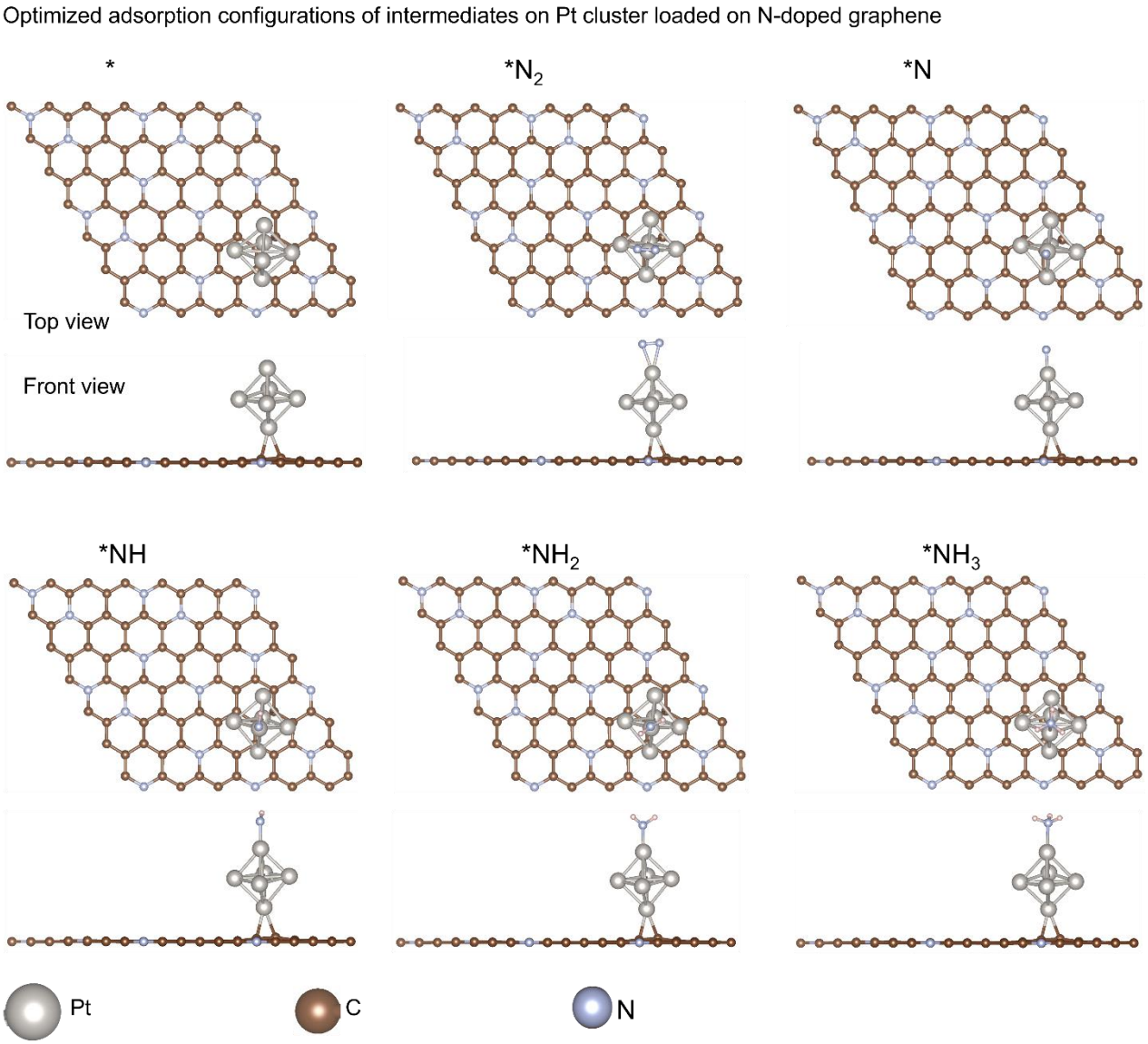

Figure S46. Optimized adsorption configurations of nitrogen-containing intermediates on a Pt cluster site.
Optimized structures of *, *N_2, *N, *NH, *NH_2, and *NH_3 intermediates on a Pt cluster anchored on N-doped graphitic carbon. Top and front views are shown for each intermediate. Grey, brown, and light blue spheres represent Pt, C, and N atoms, respectively.

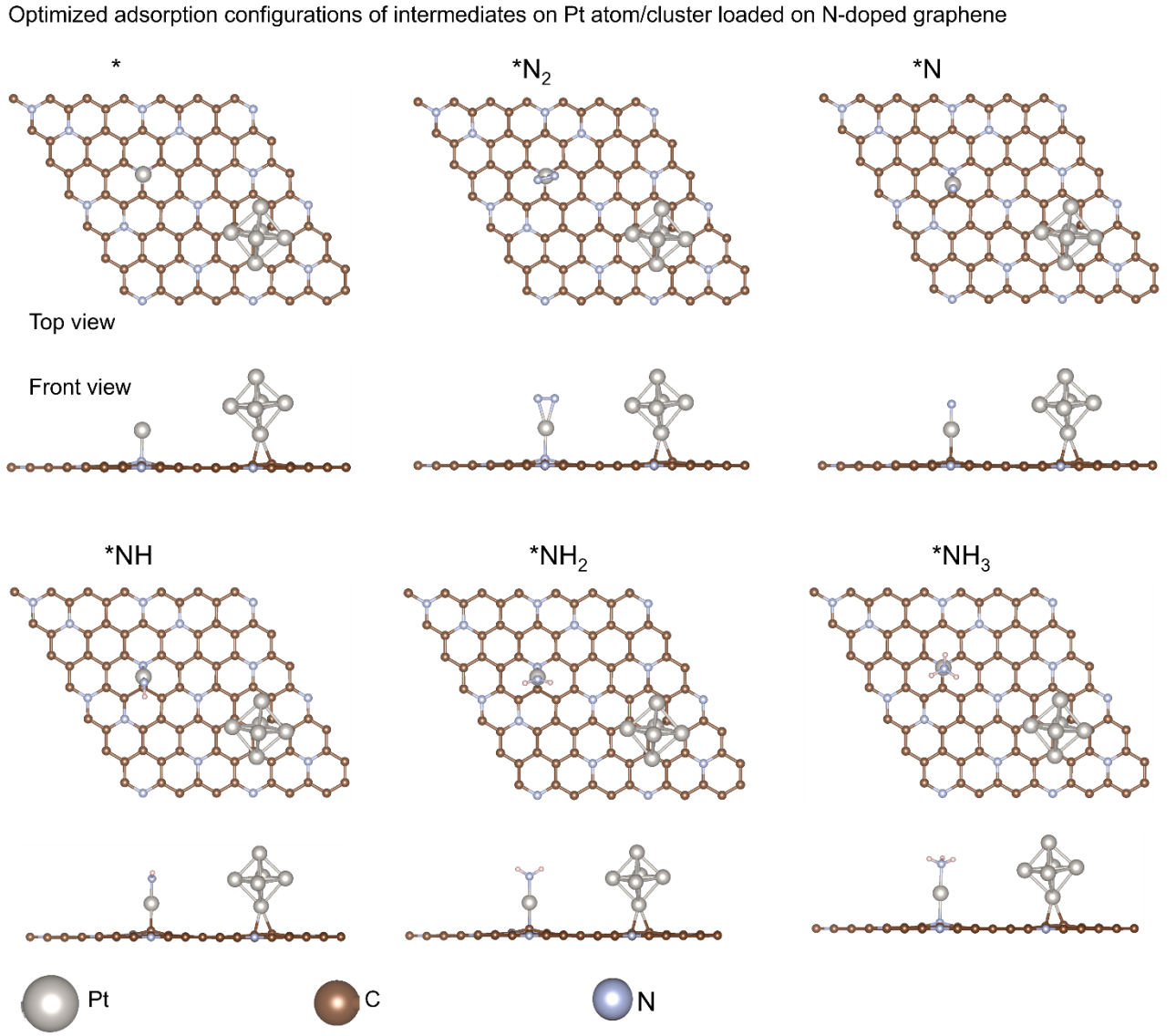

Figure S47. Optimized adsorption configurations of nitrogen-containing intermediates on coupled Pt single-atom/Pt-cluster sites.

Optimized structures of *, *N_2, *N, *NH, *NH_2, and *NH_3 intermediates on the coupled Pt single-atom/Pt-cluster structure anchored on N-doped graphitic carbon. Top and front views are shown for each intermediate. Grey, brown, and light blue spheres represent Pt, C, and N atoms, respectively.

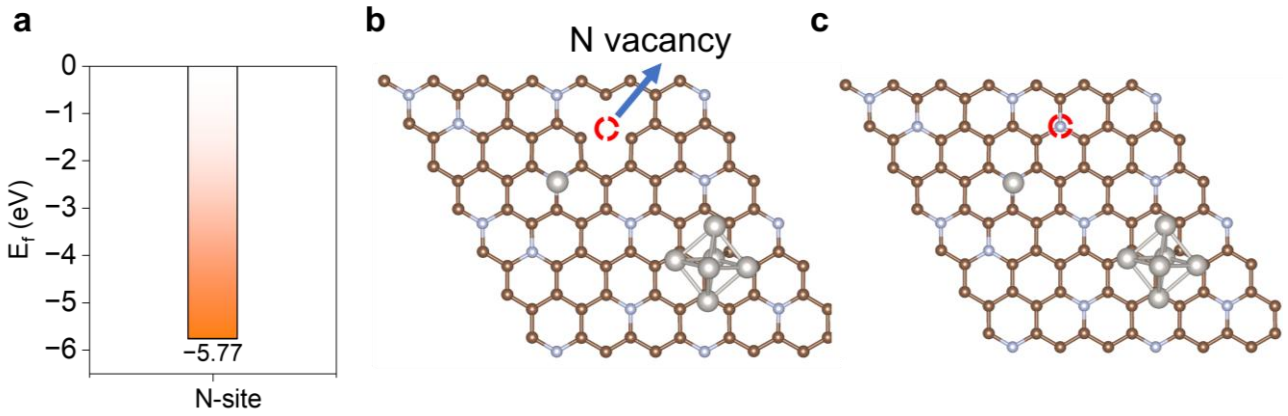

Figure S48. DFT analysis of N-vacancy replenishment in Pt–N_x–C motifs. (a) Formation energy for filling an N vacancy in the Pt–N_x–C motif by an N species generated on an isolated Pt site. (b) Optimized structure with an N vacancy in the Pt–N_x–C motif. (c) Optimized structure after N-vacancy replenishment.

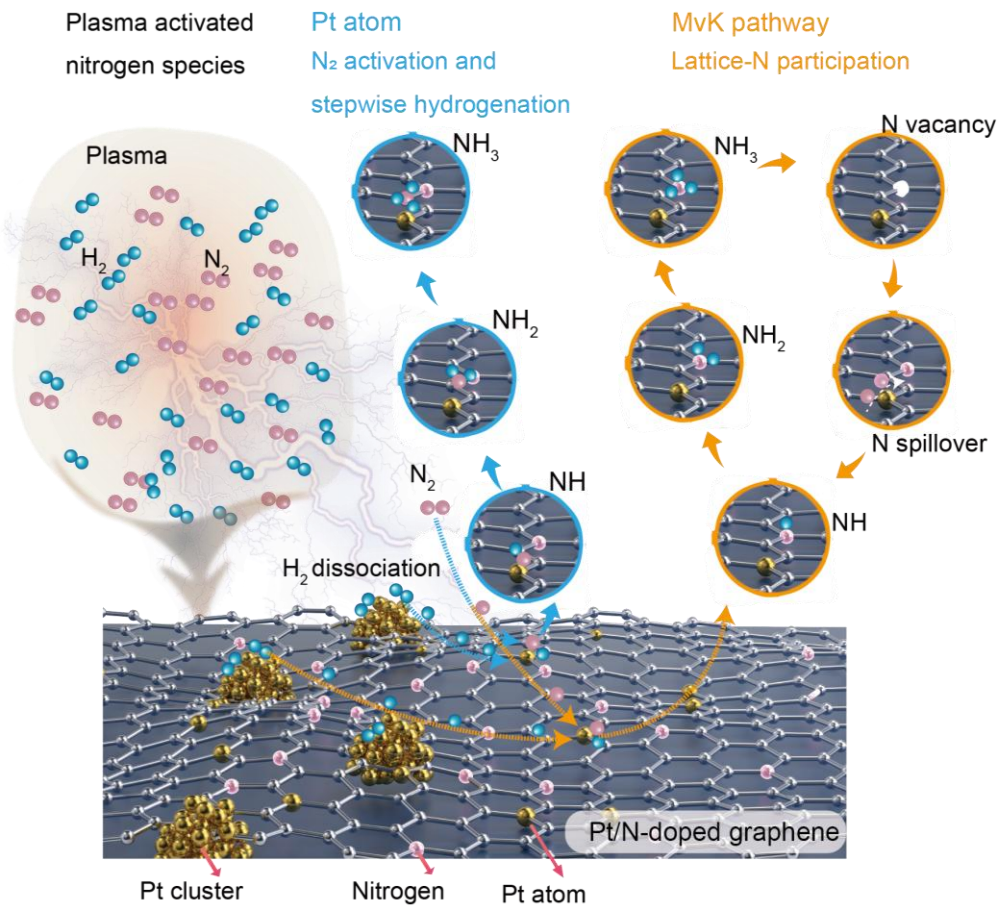

Figure S49. Schematic representation of proposed reaction pathways for plasma-catalytic NH_3 synthesis catalyzed by Pt/N-doped graphitic carbon. Schematic illustration of NH_3 formation catalyzed by Pt/N-doped graphitic carbon, involving plasma-activated nitrogen species, Pt-assisted N_2 activation and hydrogenation, H_2 dissociation on Pt clusters, and lattice-N participation through an N-vacancy-mediated Mars–van Krevelen-like pathway.

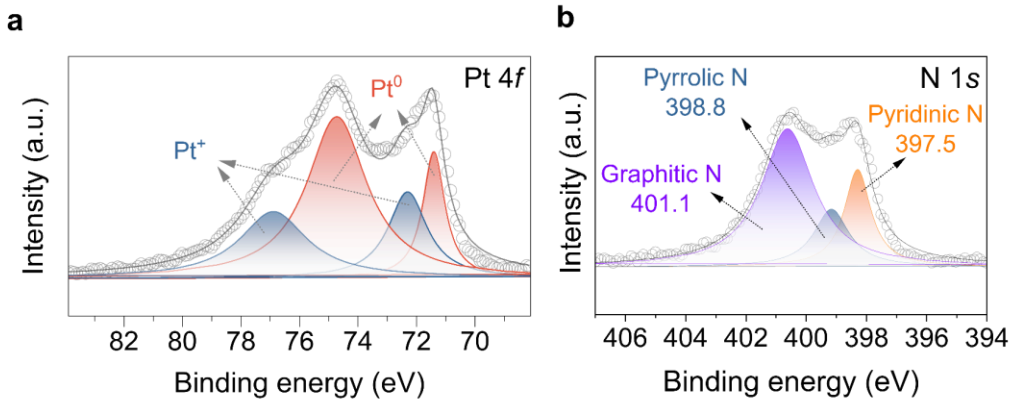

Figure S50. XPS data characterizing Pt/N-doped graphitic carbon after 85 h of plasma-catalytic NH_3 synthesis. (a) Pt 4f spectra showing Pt^0 (61.6 at.%) and Pt^+ (37.4 at.%) species. (b) N 1s spectra consisting of pyrrolic N (22.3 at.%), graphitic N (60.3 at.%), and pyridinic N (17.4 at.%). For comparison, the fresh catalyst contained Pt^0 (64.8 at.%) and Pt^+ (34.2 at.%), Figure 2g, together with pyrrolic N (14.7 at.%), graphitic N (52.5 at.%), and pyridinic N (32.8 at.%), Figure 2d.

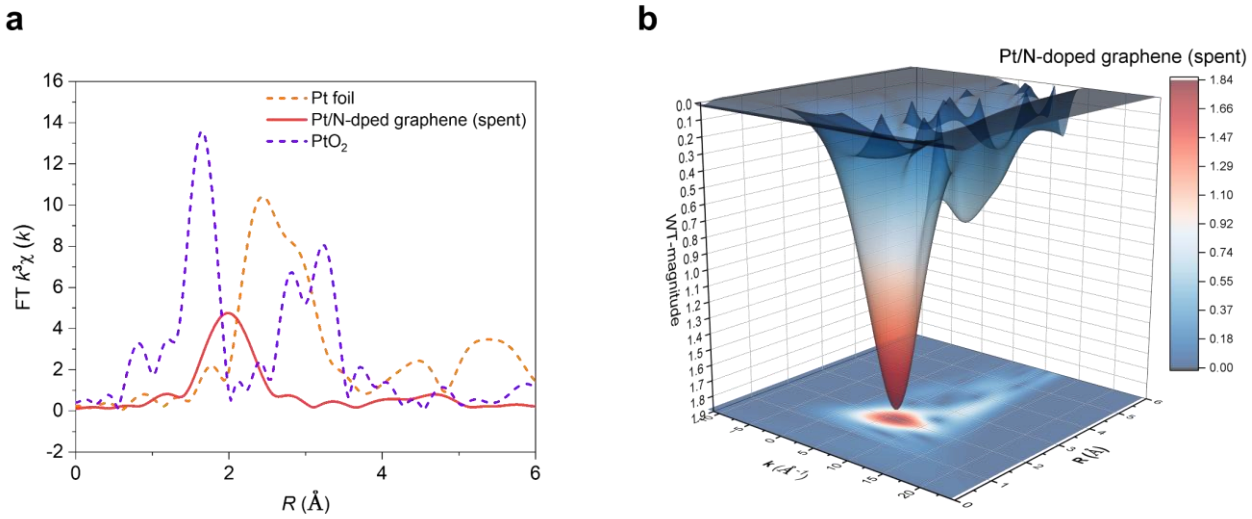

Figure S51. EXAFS characterization of spent Pt/N-doped graphene. (a) FT-EXAFS spectra of spent Pt/N-doped graphene compared with Pt foil and PtO_2 references. (b) Corresponding WT-EXAFS contour plot of the spent Pt/N-doped graphene catalyst.

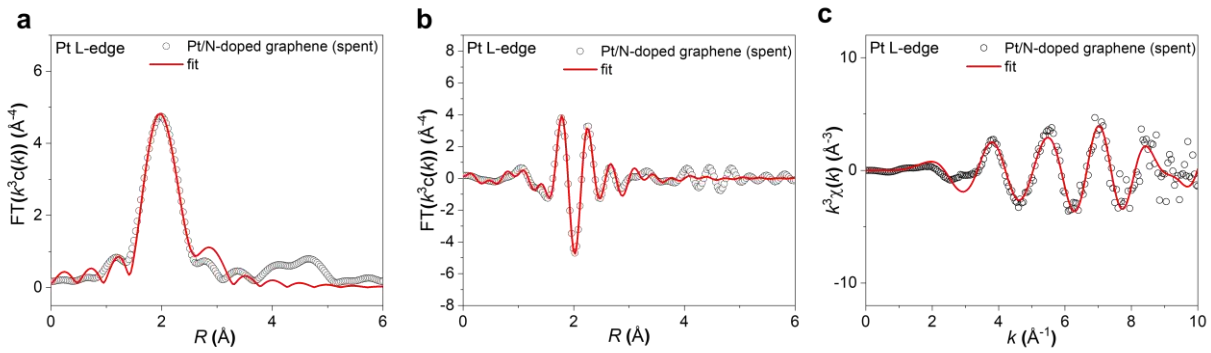

Figure S52. EXAFS fitting results at the Pt L_3-edge characterizing Pt supported on N-doped graphitic carbon after reaction. (a) R-space magnitude of the Fourier-transformed EXAFS spectra; (b) imaginary part of the R-space EXAFS fitting; (c) k^3-weighted $\chi(k)$ fitting in k-space. Open symbols represent experimental results, and red lines correspond to the best fits.

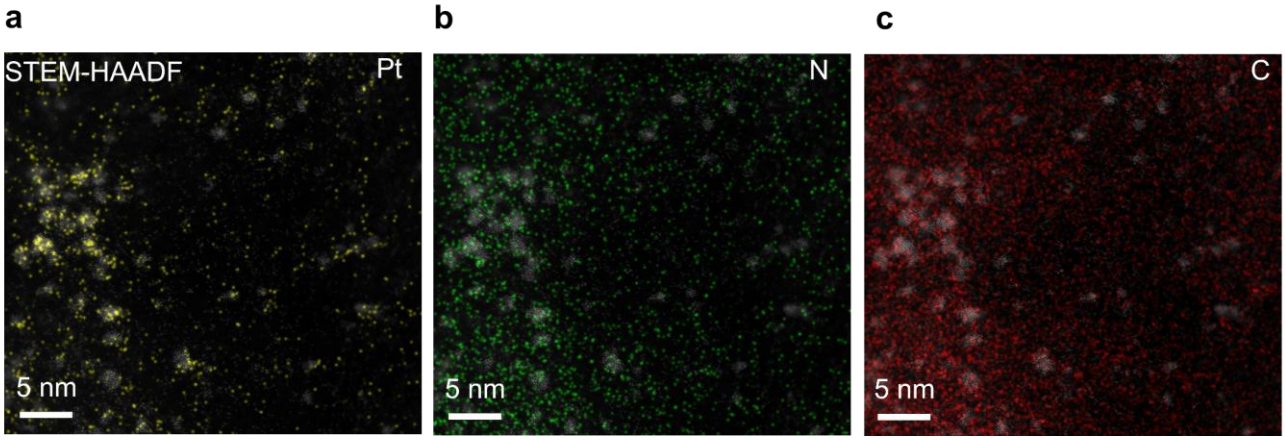

Figure S53. STEM–EDX elemental mapping of the used Pt/N-doped graphitic carbon catalyst after plasma-catalytic ammonia synthesis. (a) Pt, (b) N, and (c) C elemental distributions. Pt species remained uniformly distributed across the N-doped graphitic carbon support after reaction, without observable formation of large Pt aggregates, indicating the structural stability of the catalyst under plasma-catalytic ammonia synthesis conditions.

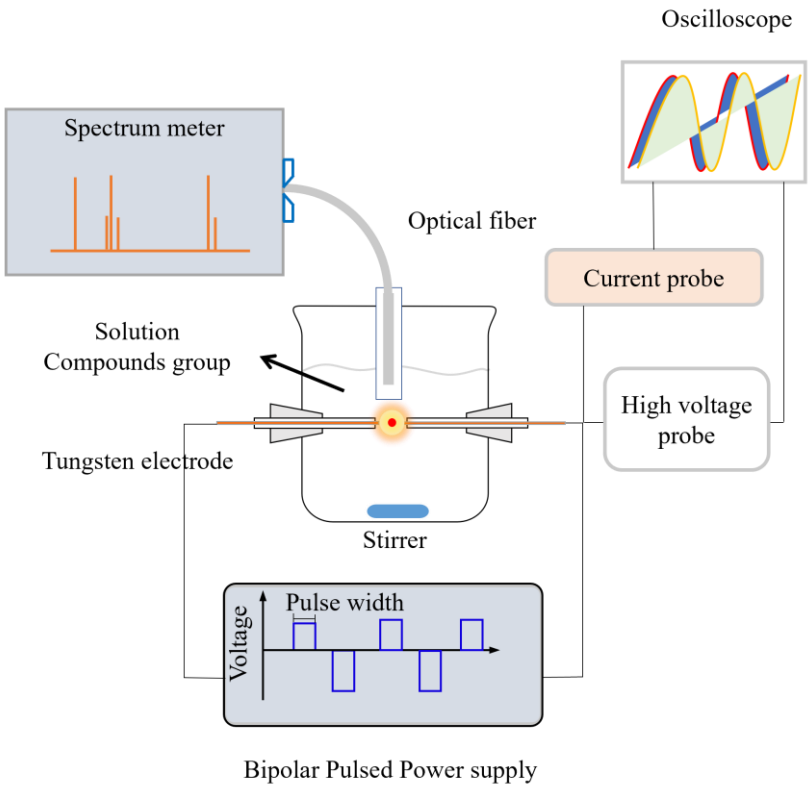

Figure S54. Schematic representation of the experimental apparatus. Experimental conditions: bipolar pulsed excitation with peak voltage of 2 kV, frequency of 100 kHz, pulse width of 1 µs, electrode gap of 1 mm, precursor volume of 100 mL.

Table S1. Physicochemical and electronic parameters of the 53 molecular precursors used in this investigation.

No.	Name	Formula	Molecular weight	Molar volume, mL mol^{-1}	Melting point, °C	Boiling point, °C	Density of liquid, g mL^{-1}	Heat of formation, kJ mol^{-1}	Total energy, eV	Electronic energy, eV	Ionization potential, eV	HOMO energy, eV	LUMO energy, eV	Dipole moment, *D*
1	benzene	C_6H_6	78.11	88.9	5.50	80.00	0.88	96.05	-817.56	-3251.15	9.82	-9.82	0.24	0.00
2	Toluene	C_7H_8	92.14	106.3	-95.00	110.00	0.87	55.21	-967.72	-4275.01	9.43	-9.43	0.32	0.65
3	Benzonitrile	C_6H_5CN	103.12	103.1	13.00	188.00	1.01	223.98	-1112.57	-4630.17	10.33	-10.33	-0.84	4.23
4	Aniline	$C_6H_5NH_2$	93.13	30.57	-6.00	184.70	1.02	88.78	-1017.53	-4332.29	8.46	-8.46	0.33	1.76
5	Nitrobenzene	C_6H_5NO2	123.11	102.3	6.00	210.00	1.21	76.06	-1578.01	-6650.59	10.73	-10.73	-1.32	5.06
6	Phenol	C_6H_5OH	94.11	89	40.90	181.80	1.05	-92.71	-1113.02	-4432.63	9.24	-9.24	0.04	1.31
7	Pyridine	C_5H_5N	79.10	80.5	-42.00	115.00	0.98	132.79	-867.33	-3305.46	10.24	-10.24	-0.26	2.38
8	3-Methylpyridine	C_6H_7N	93.13	98	2.4	145.00	0.96	92.32	-1017.49	-4332.62	9.84	-9.84	-0.15	2.77
9	3-Cyanopyridine	$C_6H_4N_2$	107.15	116.3	−15	163.00	0.95	48.78	-1167.68	-5461.67	9.58	-9.58	0.05	1.36
10	3-Aminopyridine	$NH_2C_5H_4N$	104.11	96.3	27.00	215.00	1.08	267.50	-1162.27	-4687.98	10.73	-10.73	-1.26	3.61
11	2,6-Lutidine	C_7H_9N	94.11	75.3	58.10	210.60	1.00	131.44	-1067.24	-4390.08	8.79	-8.79	-0.10	3.61
12	2,4,6-Trimethylpyridine	$C_8H_{11}N$	121.18	133.2	−43	172.00	0.92	6.56	-1317.85	-6673.25	9.52	-9.52	0.17	1.94
13	Pyrazine	$C_4H_4N_2$	80.09	77.7	54.00	118.00	1.03	185.54	-916.94	-3360.19	10.24	-10.24	-0.80	0.00
14	2-Methylpyrazine	$C_5H_6N_2$	94.11	91.4	−29	135.00	1.03	143.65	-1067.11	-4393.30	10.07	-10.07	-0.63	0.94
15	2,5-Dimethylpyrazine	$C_6H_8N_2$	108.14	109.7	15.00	182.00	0.99	102.60	-1217.28	-5508.22	9.85	-9.85	-0.48	0.09

16	Cyanopyrazine	$C_5H_3N_3$	98.19	128.4	-127.00	100.00	0.77	-141.80	-1049.72	-5499.49	10.66	-10.66	3.95	0.08
17	Pyrrole	C_4H_5N	86.13	90.8	−19	140.00	0.95	-272.18	-1045.10	-4476.14	10.50	-10.50	3.08	2.05
18	1-Methylpyrrole	C_5H_7N	84.16	108.7	6.00	81.00	0.78	-114.77	-899.71	-4340.29	10.81	-10.81	4.13	0.00
19	2,5-Dimethylpyrrole	C_6H_9N	84.16	112.1	−142	72.00	0.75	-110.40	-899.66	-4295.31	11.01	-11.01	3.79	0.11
20	Pyrazole	$C_3H_4N_2$	71.12	82.1	-63.00	88.00	0.86	-23.30	-799.17	-3298.55	9.22	-9.22	3.09	2.01
21	3-Methylpyrazole	$C_4H_6N_2$	85.15	106.6	-90.00	76.00	0.80	-30.13	-948.98	-4395.96	8.88	-8.88	2.98	1.83
22	3-Aminopyrazole	C_3H_5N3	99.13	96.2	-24.00	202.00	1.03	-206.37	-1217.66	-5295.76	9.12	-9.12	1.65	4.39
23	3-Amino-5-methylpyrazole	$C_4H_7N_3$	99.18	114.7	18.00	135.00	0.87	-94.09	-1099.38	-5551.84	9.33	-9.33	3.45	1.90
24	1-Methylimidazole	$C_4H_6N_2$	83.09	90	35.00	282.00	1.00	197.73	-993.61	-3726.58	8.68	-8.68	0.59	2.00
25	1,2-Dimethylimidazole	$C_5H_8N_2$	70.14	94.1		50.00	0.75	-83.59	-749.64	-3242.61	11.03	-11.03	3.88	0.02
26	1H-1,2,3-Triazole	$C_2H_3N_3$	97.12	90	47.00	213.00	1.00	156.02	-1143.79	-4780.93	8.55	-8.55	0.76	2.70
27	Cyclopentane	C_5H_{10}	85.15	99.0	-86.00	108.00	0.86	-62.98	-949.32	-4344.59	9.38	-9.38	3.37	1.87
28	Methylcyclopentane	$C_5H_9CH_3$	69.07	58.2	22.00	203.00	1.19	248.66	-843.35	-2767.50	10.57	-10.57	-0.12	4.63
29	Cyclopentylamine	$C_5H_9NH_2$	67.09	69.5	-23.00	130.00	0.97	110.70	-744.47	-2666.88	9.02	-9.02	1.00	2.26
30	Cyclopentanol	C_5H_9OH	114.19	122.8	-49.90	171.00	0.93	-319.73	-1345.06	-6977.07	10.23	-10.23	2.97	2.02
31	Pyrrolidine	C_4H_9N	95.15	101.3	7.70	169.00	0.94	31.54	-1044.77	-4677.13	8.37	-8.37	1.26	2.67
32	2-Pyrrolidone	C_4H_7NO	112.22	143.4	-37.00	126.00	0.77	-168.69	-1199.73	-6739.34	10.56	-10.56	3.84	0.00

33	1-Methylpyrrolidine	$C_5H_{11}N$	99.18	121.2	-5.00	127.00	0.84	-65.07	-1099.08	-5556.85	8.91	-8.91	3.28	1.59
34	1-Methyl-2-pyrrolidone	C_5H_9NO	81.12	89.9	-57.00	113.00	0.91	107.67	-894.25	-3642.39	8.84	-8.84	1.17	3.07
35	Cyclohexane	C_6H_{12}	82.11	77.2	13.00	204.00	1.02	151.15	-943.95	-3672.62	9.61	-9.61	0.62	1.73
36	Methylcyclohexane	C_7H_{14}	114.19	120.1	41.00	376.00	0.95	-76.31	-1299.07	-6915.46	9.17	-9.17	3.14	3.18
37	Cyclohexylamine	$C_6H_{13}N$	85.15	98.9	-7.00	106.00	0.86	-38.44	-949.07	-4396.82	8.91	-8.91	3.30	1.66
38	1,4-Dimethylcyclohexane	C_8H_{16}	113.20	130.4	-8.50	150.00	0.86	-116.58	-1249.34	-6857.02	9.27	-9.27	3.45	1.77
39	2-Methylcyclohexylamine	$C_7H_{15}N$	105.10	85.7	21.00	87.00	1.17	341.47	-1211.66	-4748.68	10.83	-10.83	-1.71	3.77
40	1,2-Cyclohexanediamine	$C_6H_{14}N_2$	85.11	76.9	24.00	245.00	1.12	-208.08	-1067.94	-4129.88	9.70	-9.70	1.50	4.52
41	2-Methylcyclohexanol	$C_7H_{14}O$	82.11	79.8	-60.00	198.00	1.04	134.40	-944.12	-3693.19	9.39	-9.39	0.67	5.02
42	1,2,4-Trimethylcyclohexane	C_9H_{18}	126.24	163.5	-50.00	145.00	0.79	-191.78	-1349.70	-8135.63	10.50	-10.50	3.80	0.08
43	Piperidine	$C_5H_{11}N$	115.18	117.5	27.00	105.00	0.98	-224.10	-1394.23	-6985.30	8.91	-8.91	2.80	2.94
44	4-Methylpiperidine	$C_6H_{13}N$	68.08	68	71.00	188.00	1.03	187.40	-793.83	-2716.16	10.01	-10.01	0.49	2.41
45	4-Aminopiperidine	$C_5H_{12}N_2$	115.18	120.4	-20.00	175.00	0.96	85.39	-1347.55	-7025.18	8.56	-8.56	2.33	1.12
46	3,5-Dimethylpiperidine	$C_7H_{15}N$	99.18	121.5	-5.00	107.00	0.82	-48.36	-1098.90	-5576.34	8.70	-8.70	3.06	1.56
47	1-Methylpiperidine	$C_6H_{13}N$	113.20	142.5	-20.00	144.00	0.83	-94.43	-1249.12	-6814.90	8.90	-8.91	3.25	1.77
48	1-Aminopiperidine	$C_5H_{12}N_2$	129.21	140.6	-27.00	65.00	0.92	25.08	-1497.90	-8603.09	8.69	-8.69	2.44	2.83
49	4-Hydroxy-1-methylpiperidine	$C_6H_{13}NO$	100.17	107.9	57.00	146.00	0.93	30.46	-1148.24	-5628.66	8.45	-8.45	2.58	0.61

50	1-Methylpiperazine	$C_5H_{12}N_2$	114.19	134	-1.00	133.00	0.85	5.62	-1298.23	-6970.94	8.60	-8.60	2.73	2.84
51	1-Amino-4-methylpiperazine	$C_5H_{13}N_3$	100.17	111.3	-5.00	137.00	0.91	11.38	-1148.44	-5640.48	8.85	-8.85	2.71	2.86
52	N,N'-Dimethylpiperazine	$C_6H_{14}N_2$	96.13	97.1	37.00	205.00	1.08	96.55	-1094.25	-4800.01	9.05	-9.06	0.84	4.94
53	1,3,5-Trimethylhexahydro-1,3,5-triazine8	$C_6H_{15}N_3$	100.17	107.9	25.00	36.00	0.93	-16.81	-1148.73	-5609.70	9.06	-9.06	3.07	1.90

Table S2. Identification of transitions in the emission spectra of atoms, molecules, and radicals.

Transition band	Wavelength (nm)	Transition	Species
Swan system	516.5, 471.5, 547.0, 558.0	$d^3\Pi_g$ - $a^3\Pi_u$	C_2
Swan system under high pressure	589.9	$d^3\Pi_g$ - $a^3\Pi_u$	C_2
Deslandres d'Azambuja system	385.2, 360.7, 358.7	$c^1\Pi_g$ - $b^1\Pi_u$	C_2
Violet system	388.3, 415.2	$B^2\Sigma^+$ - $X^2\Sigma^+$	CN
Carbon molecule anion	545.3	$^2\Sigma$ - $^2\Sigma$	C_2^-
Fulcher α hydrogen molecule	600 - 630	$d^3\Pi^-_u$ - $a^3\Sigma_g^+$	C_2
Balmer series	656.0, 486.1, 434.0	n=5-2, 4-2, 3-2	H_α, H_β, H_γ
Oxygen	777, 844.6	^5P - $^5S_0$, ^3P - $^3S_0$	O

Table S3. EXAFS fitting parameters.

Sample	S_0^2	Scattering path	CN*	*R*(Å)	σ^2 (10^{-3} Å^2)	ΔE_0	R factor
Pt foil	0.95	Pt−Pt	12	2.75 ± 0.01	5.9 ± 0.4	6.71 ± 0.54	0.0149
Pt/N-doped graphene	0.95	Pt−N	5.6	2.21 ± 0.01	0.4 ± 0.1	9.83 ± 0.35	0.0020
		Pt−Pt	1.2	2.91 ± 0.01	13.4 ± 0.1		
Pt/N-doped graphene (used catalyst)	0.95	Pt−N	5.9	2.49±0.01	2.1 ± 0.1	4.15±1.72	0.0169
		Pt−Pt	1.9	2.71±0.02	4.0 ± 0.1		
PtO_2	0.95	Pt−O	6.0	1.98 ± 0.01	3.7 ± 0.3	9.32 ± 0.01	0.0018
		Pt−Pt	6.0	3.07 ± 0.01	3.4 ± 0.7		
		Pt−Pt	8.0	3.49 ± 0.01	10.6 ± 1.8		
		Pt−O	10.0	3.58 ± 0.01	1.8±0.1		

CN: coordination number; *R*: absorber-backscatterer distance; σ^2: Debye–Waller factor (disorder term); ΔE_0: inner potential correction; R factor: goodness of fit. The asterisk indicates the fitted coordination number.

EXAFS fitting was performed using k^3-weighted spectra. In fitting data characterizing the Pt/N-doped graphitic carbon sample, the *k* range was ~3.0–9.5 Å^{-1}, and the *R* range ~1.0–3.0 Å, with an error bound of ±0.01 Å for the fitted bond distances. The fitting of data characterizing Pt foil was performed over a *k* range of ~3.0–11.0 Å^{-1} and an *R* range of ~1.0–3.0 Å, with an error bound of ±0.01 Å. The fitting characterizing PtO_2 was performed over a *k* range of ~3.0–10.0 Å^{-1} and an *R* range of ~1.0–4.0 Å, with an error bound of ±0.01 Å. The amplitude reduction factor S_0^2 was fixed at 0.95.

Table S4. Summary of reactor configuration, packing protocol, operating conditions, and discharge characteristics for plasma-catalytic NH_3 synthesis.

Component of reactor system/operating parameter/observation	Pt/N-doped graphitic carbon	Commercial N-doped graphene	Commercial Pt/XC72	Plasma only
Reactor geometry	Coaxial packed-bed DBD quartz tube			
Quartz tube	OD 8 mm, ID 6 mm			
HV electrode	1.5 mm W rod			
Catalyst amount	100 mg catalyst + 200 mg quartz sand			No catalyst/sand
Particle size	30–40 mesh			N.A.
Packed/discharge length	7 cm	10 cm	17 cm	7 cm
Feed gas	N_2/H_2 = 1:1			
Total flow rate	20 mL(NTP) min^{-1}			
Pressure	Atmospheric pressure			
Frequency	~8 kHz			
Voltage range	6–9 kV			
Power at 6 kV	3.88 W	3.52 W	3.05 W	3.89 W
Power at 7 kV	4.13 W	4.37 W	4.01 W	3.99 W
Power at 8 kV	4.41 W	4.90 W	4.12 W	4.11 W
Power at 9 kV	4.55 W	5.62 W	4.36 W	5.32 W
V–I waveform	Stable periodic DBD; current peak ~10–15 mA	Stable periodic DBD; current peak ~12–22 mA	Stable periodic DBD; current peak ~6–8 mA	Stable periodic DBD; current peak ~6–20 mA
OES features	Dominant N_2 bands; weak Hα at high voltage			
IR temperature range	Max. ~51.0–86.0 °C	Max. ~54.1–127 °C	Max. ~45.7–76.1 °C	Max. ~58.2–137 °C

Table S5. Comparison of plasma-catalytic NH_3 synthesis performance and key operating conditions reported in this work and previous studies.

Catalyst / System	Reactor type	Mass of packing	Discharge mode	Feed gas composition (molar)	Total flow rate mL(NTP) min^{-1}	Frequency / Voltage	Discharge power	NH_3 concentration	NH_3 synthesis rate	NH_3 production rate / STY	Energy yield	SEI	Reference
Ni/LaOF	DBD	0.1 g	AC; CTP-2000K	N_2/H_2 = 1:3	25	7.87 kHz; 5–10 kV	3, 6, and 13 W investigated; best reported performance at 13 W	n.r.	34.94 µmol min^{-1} $g\text{-}cat^{-1}$ at 13 W		2.7 g-NH_3 kWh^{-1} at 13 W	31.2 kJ L^{-1}	[5]
LDH	DBD	~200 mg	AC H.V. power supply, PSPT-2000C	N_2/H_2 = 1:1	20	8.1 kHz; 12 kV	~13 W	n.r.	4.42–4.52 mmol g^{-1} h^{-1}	4.42–4.52 mmol g^{-1} h^{-1}, mass-normalized to packed material	1.67–1.71 gNH_3 kWh^{-1}	~39 kJ L^{-1}	[6]
MCM-41	DBD	0.5 g	n.r.	N_2/H_2 = 1:3	40 for main low-flow tests; up to 1200 in high-flow tests	n.r.	24 W at SEI = 36 kJ L^{-1} and 40 mL min^{-1}; 40 W at SEI = 60 kJ L^{-1} and 40 mL min^{-1}	27115 ppm at low flow; NH_3 yield 5.3%	3959 µmol g^{-1} h^{-1} at SEI = 36 kJ L^{-1}	3959 µmol g^{-1} h^{-1}; total rate ~ 1979.5 µmol h^{-1} based on 0.5 g catalyst	1.2 gNH_3 kWh^{-1} at SEI = 24 kJ L^{-1}; up to 3.9 gNH_3 kWh^{-1} at 1.2 L min^{-1} high-flow operation	24–60 kJ L^{-1}; main catalytic comparison at 36 kJ L^{-1}	[7]
Ru/Al_2O_3	DBD	3.6 g	AC; customized HV power supply	N_2/H_2 = 2:1	120	20 kHz; 8–9 kV	38.4 W	1.49%	~20.1 µmol min^{-1} $gcat^{-1}$, calculated	~72.4 µmol min^{-1} total; ~1.21 mmol $gcat^{-1}$ h^{-1}, calculated	~1.89 gNH_3 kWh^{-1}, calculated from 32.39 MJ mol^{-1}	~19.2 kJ L^{-1}	[8]
PZT ferroelectric pellets	DBD	n.r.	DBD; Stanford Research Systems DS345 function generator	N_2/H_2 = 1:3	11.5	500 Hz; applied voltage typically 3–7 kV depending on gap	n.r.	n.r.	n.r.	NH_3 production up to 0.34 mL min^{-1}	0.9 gNH_3 kWh^{-1} at residence time = 8.8 s; 0.55 gNH_3 kWh^{-1} at 10 mm gap	n.r.	[9]
Zeolite 4A in-situ NH_3 adsorption	DBD	600 mg	AC; PMV 500–4000 power supply	$H_2:N_2$ = 1:2 for highest energy yield; $H_2:N_2$ = 4:1, 2:1, 1:1, 1:2, 1:4 also tested	10	25 kHz; Up to 10 kV	6.4 W	0.1–0.2 mol% before breakthrough and ~1.3 mol% after saturation for $H_2:N_2$ = 1:4 example	n.r.	Cumulative NH_3 yield reported for 5 and 75 min experiments	2.3 gNH_3 kWh^{-1} for in situ removal; 1.1 gNH_3 kWh^{-1} for steady-state operation	38.4 kJ L^{-1}	[10]
Co–Ni/Al_2O_3	DBD	2 g	AC; CTP-2000K, 40 kHz	N_2/H_2 = 1:1	200	40 kHz	30.81 W output power; 20 W also reported for comparison point	n.r.	1500 µmol g^{-1} h^{-1}	3000 µmol h^{-1} at 30.81 W; 960 µmol h^{-1} at 20 W	0.83 gNH_3 kWh^{-1} at 30.81 W; 1.28 gNH_3 kWh^{-1} at 20 W	9.24 kJ L^{-1} at 30.81 W / 200 mL min^{-1}; 6.0 kJ L^{-1} at 20 W / 200 mL min^{-1}	[11]

Zeolite 5A	DBD	0.1 g	Atmospheric DBD; high-voltage power supply; frequency ~25 kHz	N_2/H_2 = 1:1 for highest rate and energy yield; N_2/H_2 = 1:6 for highest NH_3 yield; 3:1–1:6 tested	25	25 kHz	9–17 W; average 13.3 ± 2.7 W; ~17 W by capacitor method at N_2/H_2 = 1:6	n.r.	15.5 μmol min^{-1} $gcat^{-1}$ at N_2/H_2 = 1:1	10.7 μmol min^{-1} total at N_2/H_2 = 1:6	15.5 gNH_3 kWh^{-1} at N_2/H_2 = 1:1; 9 gNH_3 kWh^{-1} at N_2/H_2 = 1:6	n.r.	[12]
K-Ru/G	DBD	~100 mg	AC	N_2/H_2 = 1:1	140	n.r.	42 W for main comparison	n.r.	13953 μmol $gcat^{-1}$ h^{-1}	~1395 μmol h^{-1}, calculated from 100 mg catalyst	5.80 gNH_3 kWh^{-1}	n.r.	[13]
Ru–Co/AC	DBD	100 mg	AC; CTP-2000K	N_2/H_2 = 1:1	120 for highest rate; 40 for ratio and power tests	~9.7 kHz	40 W for highest rate/EE; 24–52 W	n.r.	7547 μmol g^{-1} h^{-1}	~754.7 μmol h^{-1}, 100 mg catalyst	3.21 gNH_3 kWh^{-1}	20 kJ L^{-1}, from 40 W / 120 mL min^{-1}	[14]
$La(OH)_3$	DBD	100 mg	AC; CTP-2000K	N_2/H_2 = 1:3	25	7.78 kHz; 5–10 kV	13 W for optimal condition	3570 ppm; 3842 ppm after 5 min H_2 plasma treatment	37.13 – 40.00 μmol min^{-1} $gcat^{-1}$	~3.71 μmol min^{-1} total, calculated from 100 mg catalyst	2.91 gNH_3 kWh^{-1} $gcat^{-1}$ as reported	31.2 kJ L^{-1}	[15]
Co–Ni/MOF-74	DBD	0.5 g	AC; CTP-2000K	N_2/H_2 = 1:1	200	40 kHz	~110.9 W, from SEI = 33.27 kJ L^{-1} and 200 mL min^{-1}	n.r.	2608.70 μmol g^{-1} h^{-1}	~1304 μmol h^{-1}, calculated from 0.5 g catalyst	0.72 gNH_3 kWh^{-1}	33.27 kJ L^{-1}	[16]
Ru-Ni/$BaTiO_3$	DBD	0.4 g	AC; CTP-2000K	N_2/H_2 = 1:1	100	9.4–9.8 kHz	5–25 W; highest NH_3 concentration at 25 W	3895 ppm at 25 W; 3083 ppm at 15 W; 994 ppm at 5 W	n.r.	n.r.	0.39 gNH_3 kWh^{-1} at 10 W; 0.26 gNH_3 kWh^{-1} at 25 W	6.0 kJ L^{-1} at 10 W; 15.0 kJ L^{-1} at 25 W	[17]
ZIF-67 with Ar dilution	DBD	100 mg	AC; high-voltage power supply	$N_2/H_2/Ar$ = 1:1.5:1.5	25	25 kHz; 7–21 kV	figure labels show ~15.5–17.8 W range under Ar conditions	n.r.	41.68 μmol min^{-1} $gcat^{-1}$	~4.17 μmol min^{-1} total, calculated from 100 mg catalyst	~2.5–2.6 gNH_3 kWh^{-1}, figure-derived from SI Fig. S6	42.81 kJ L^{-1}	[18]
Pt/N-doped graphitic carbon	DBD	300 mg	AC; CTP-2000K	N_2/H_2 = 1:1	20	8 kHz; 6 kV	3.88 W	0.22%	18.3 μmol min^{-1} $gcat^{-1}$	109.8 μmol h^{-1}	0.481 gNH_3 kWh^{-1}	11.64 kJ L^{-1}	This work
						8 kHz; 7 kV	4.13 W	0.75%	62.2 μmol min^{-1} $gcat^{-1}$	373.5 μmol h^{-1}	1.541 gNH_3 kWh^{-1}	12.39 kJ L^{-1}	
						8 kHz; 8 kV	4.41 W	1.65%	137 μmol min^{-1} $gcat^{-1}$	822.1 μmol h^{-1}	3.175 gNH_3 kWh^{-1}	13.23 kJ L^{-1}	
						8 kHz; 9 kV	4.55 W	2.13%	177 μmol min^{-1} $gcat^{-1}$	1061.1 μmol h^{-1}	3.970 gNH_3 kWh^{-1}	13.65 kJ L^{-1}	

Supplementary References

1 G. Kresse, J. F. l. Efficient iterative schemes for ab initio total-energy calculations using a plane-wave basis set. *PHYSICAL REVIEW B* **54** (1996).

2 G. Kresse, D. J. From ultrasoft pseudopotentials to the projector augmented-wave method. *PHYSICAL REVIEW B* **59** (1999).

3 John P. Perdew, K. B., Matthias Ernzerhof. Generalized Gradient Approximation Made Simple. *PHYSICAL REVIEW LETTERS* (1996).

4 Dal Corso, A. Pseudopotentials periodic table: From H to Pu. *Computational Materials Science* **95**, 337-350 (2014). https://doi.org/10.1016/j.commatsci.2014.07.043

5 Li, K., Chen, S., Wang, H. & Wang, F. Plasma-assisted ammonia synthesis over Ni/LaOF: Dual active centers consisting of oxygen vacancies and Ni. *Applied Catalysis A: General* **650** (2023). https://doi.org/10.1016/j.apcata.2022.118983

6 Zhang, Y. *et al.* MgAl layered double hydroxide (LDH) for promoting ammonia synthesis in non-thermal plasma: Role of surface oxygen vacancy. *Chemical Engineering and Processing - Process Intensification* **195** (2024). https://doi.org/10.1016/j.cep.2023.109608

7 Wang, Y. *et al.* Shielding Protection by Mesoporous Catalysts for Improving Plasma-Catalytic Ambient Ammonia Synthesis. *J Am Chem Soc* **144**, 12020-12031 (2022). https://doi.org/10.1021/jacs.2c01950

8 Li, S., van Raak, T. & Gallucci, F. Investigating the operation parameters for ammonia synthesis in dielectric barrier discharge reactors. *Journal of Physics D: Applied Physics* **53** (2020). https://doi.org/10.1088/1361-6463/ab4b37

9 Gómez-Ramírez, A., Cotrino, J., Lambert, R. M. & González-Elipe, A. R. Efficient synthesis of ammonia from N2and H2alone in a ferroelectric packed-bed DBD reactor. *Plasma Sources Science and Technology* **24** (2015). https://doi.org/10.1088/0963-0252/24/6/065011

10 Rouwenhorst, K. H. R., Mani, S. & Lefferts, L. Improving the Energy Yield of Plasma-Based Ammonia Synthesis with In Situ Adsorption. *ACS Sustainable Chemistry & Engineering* **10**, 1994-2000 (2022). https://doi.org/10.1021/acssuschemeng.1c08467

11 Liu, Y. *et al.* Synergistic Effect of Co–Ni Bimetal on Plasma Catalytic Ammonia Synthesis. *Plasma Chemistry and Plasma Processing* **42**, 267-282 (2022). https://doi.org/10.1007/s11090-021-10223-1

12 Shah, J. R., Gorky, F., Lucero, J., Carreon, M. A. & Carreon, M. L. Ammonia Synthesis via Atmospheric Plasma Catalysis: Zeolite 5A, a Case of Study. *Industrial & Engineering Chemistry Research* **59**, 5167-5176 (2020). https://doi.org/10.1021/acs.iecr.9b05220

13 Gao, B. *et al.* Alkali metal promoter induced Ru/G catalyst structure and electronic regulation for efficient plasma-catalytic NH3 synthesis. *Applied Catalysis B: Environment and Energy* **394** (2026). https://doi.org/10.1016/j.apcatb.2026.126833

14 Gao, B. *et al.* Insight into the effect of support properties on DBD plasma-catalytic NH3 synthesis over Ru-Co bimetallic catalysts. *Fuel* **382** (2025). https://doi.org/10.1016/j.fuel.2024.133802

15 Li, K. *et al.* Plasma-catalyzed ammonia synthesis over La(OH)3 catalyst: Effects of basic sites, oxygen vacancies, and H2 plasma treatment. *International Journal of Hydrogen Energy* **59**, 1287-1296 (2024). https://doi.org/10.1016/j.ijhydene.2024.02.123

16 Liu, Y. *et al.* Co-Ni/MOF-74 catalyst packed-bed DBD plasma for ammonia synthesis. *Plasma Processes and Polymers* **21** (2023). https://doi.org/10.1002/ppap.202300086

17 Liu, J. *et al.* Plasma-catalytic synthesis of ammonia over Ru/BaTiO3-based bimetallic catalysts: Synergistic effect from dual-metal active sites. *Fuel Processing Technology* **250** (2023). https://doi.org/10.1016/j.fuproc.2023.107851

18 Gorky, F. *et al.* Plasma-Induced Catalytic Conversion of Nitrogen and Hydrogen to Ammonia over Zeolitic Imidazolate Frameworks ZIF-8 and ZIF-67. *ACS Appl Mater Interfaces* **13**, 21338-21348 (2021). https://doi.org/10.1021/acsami.1c03115